Turbulence in Planar Taylor-Couette Flows

Undergraduate Thesis

Submitted in partial fulfillment of the requirements of
BITS F421T Thesis

By

Jayesh Sanwal
ID No. 2015A4TS0440H

Under the supervision of:

Prof. Gregory Falkovich
&
Dr. KRC Murthy

BIRLA INSTITUTE OF TECHNOLOGY AND SCIENCE PILANI, HYDERABAD CAMPUS
May 5, 2019

Declaration of Authorship

I, Jayesh Sanwal, declare that this Undergraduate Thesis titled, 'Turbulence in Planar Taylor-Couette Flows' and the work presented in it are my own. I confirm that:

- This work was done wholly or mainly while in candidature for a research degree at this University.
- Where any part of this thesis has previously been submitted for a degree or any other qualification at this University or any other institution, this has been clearly stated.
- Where I have consulted the published work of others, this is always clearly attributed.
- Where I have quoted from the work of others, the source is always given. With the exception of such quotations, this thesis is entirely my own work.
- I have acknowledged all main sources of help.
- Where the thesis is based on work done by myself jointly with others, I have made clear exactly what was done by others and what I have contributed myself.

Signed: ________________________________

Date: ________________________________

Certificate

This is to certify that the thesis entitled, "*Turbulence in Planar Taylor-Couette Flows*" and submitted by Jayesh SANWAL ID No. 2015A4TS0440H in partial fulfillment of the requirements of BITS F421T Thesis embodies the work done by him under my supervision.

Supervisor
Prof. Gregory FALKOVICH
Pollak Professorial Chair in Physics,
Weizmann Institute of Science, Israel
Date:

Co-Supervisor
Dr. KRC MURTHY
Assistant Professor,
BITS-Pilani Hyderabad Campus
Date:

BIRLA INSTITUTE OF TECHNOLOGY AND SCIENCE PILANI, HYDERABAD CAMPUS

Abstract

Bachelor of Engineering (Hons.)

Turbulence in Planar Taylor-Couette Flows

by Jayesh SANWAL

This work deals with the simulation of a 2D turbulence in Taylor-Couette flows. We investigate if a laminar flow act as a global attractor in 2D for large Reynolds number, or do other stable states exist. Since in case of channel flows, laminar flow seems to be a global attractor, the question is if shear flows themselves show such behavior in curved geometries. While working, another interesting physical observation was made about the non-monotonic relaxation to the laminar flow: Starting from values significantly higher than laminar, the total kinetic energy decreases to a lesser value and then grows back to give the laminar flow. This phenomenon is studied in some detail and a possible reason for this is then examined. The work also investigates the creation and destruction of vortices inside the domain, and draws observations based on the sign of the vortices relative to the vorticity of the laminar flow. Since the creation and subsequent death of turbulence is a very interesting observation and can only be seen in 2D, it is studied extensively.

Contents

List of Figures

List of Tables

Chapter 1

Introduction

1.1 Turbulence

In my rather limited experience with fluid dynamics, I have often faced a problem in defining and understanding the problem of turbulence, and that is what has drawn me to it for a very long time. In introductory courses to fluid dynamics, turbulence is often said to be unsteady, irregular and random in nature, and therefore extremely difficult to predict. However, the discussion beyond that is limited in its scope and nature. Stephen Pope, in his iconic book on Turbulent Flows [7] discusses this in length, and is briefly described here.

Since the word random does very little to quantify the nature of turbulence, we begin by saying that in turbulent flows, variations in the velocity field may occur significantly in both, space and time. What this effectively means is that flow steamlines are not parallel to each other, and follow different paths. Another interesting thing to note about the Navier Stokes equation is that it is dependent on initial conditions, and small perturbations in the initial conditions leads to huge changes in the flow, due to the nature of the non-linear term of the equation. This is not true in the transitional regime, or very close to the critical Re, but is true for larger values of Reynolds' numbers. Turbulence occurs when strong shear exists in between two or more adjacent layers of fluid flowing with different velocities. The difference of velocity between the layers result in the formation of local instabilities which extract the kinetic energy from the mean fluid flow. This kinetic energy is then gets transported to small-scale or perturbations, that meander away from the fluid flow, and have a tendancy to rotate, or produce vorticity (defined as the curl of the velocity vector, $\nabla \mathbf{V}$). These perturbations then either give energy to the smaller length scales, called the direct cascade, or to larger length scales, based on the level of stratification of the flow, called inverse cascades.

1.2 Planar Turbulence

The main topic of this thesis was the work on planar turbulence, or turbulence in thin films or scales where one of the spatial dimensions is negligible with respect to the other two, or the motion in the vertical direction is somehow restricted (as in the case of soap films). This allows 2D turbulence (or planar turbulence) to have huge impact on the fields of meteorology, oceanography, and also contributes to its growing application in specialised MEMS devices.

The advantage of using a 2D approximation for fluids is that the behavior of 2D flows is different from 3D flows, and therefore some phenomena can be modelled more accurately using planar turbulence. It also promises to show great applications in surgical devices and coolants, although this aspect has been not extensively covered in the literature. Not only that, planar turbulence and the inverse cascade have recently shot into greater prominence after its success in explaining formation of plumes, jets and vortices on the surface of Jupiter, as seen by the NASA spacecraft Juno. Some pictures captured by Juno are shown in 1.1.

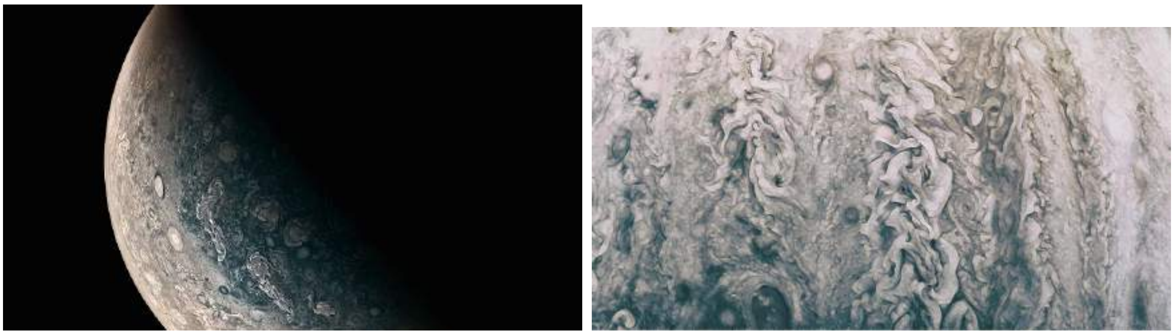

FIGURE 1.1: Pictures of Juno captured by NASA

Another aspect which initially motivated the study in planar turbulence is that it is easier to simulate on digital computers compared to 3D turbulence, and is therefore more efficient in such systems, and has proved to be a valuable testing ground for dynamical theories.

When it comes to the physical sciences, a historical perspective is often important to understand where things are in their current form, and fluid dynamics is no different. The most notable work on planar turbulence was done by Robert Kraichnan, in his landmark paper "Inertial Ranges in Two-Dimensional Turbulence" [5], for which he was also awarded the Dirac Medal. This was followed by a lot of people working on this area, and eventually producing a large and interesting body of work highlighting a few interesting features in planar turbulence. In his work, Kraichnan talks about the energy and vorticity cascades in two dimensions which can be displayed using the Navier-Stokes equation and the inviscid conservation laws. According to Kraichnan, the 2D NSE conserves energy and squared vorticity in each triad of wave-numbers, and this is arguement leads to the inverse energy cascade, which implies that the energy moves up the length scales, from smaller to larger eddies (vortices). A very elegant explanation of the paper is provided Prof. Falkovich, in Section 3.3 of his book [3], which goes as described below. We begin with the Euler equation, and the continuity equation. The non-linear term conserves the pumping and dumping, and need not be taken into account here.

$$\frac{\delta \mathbf{u}}{\delta t} + \mathbf{u}.\nabla u = -\nabla P \tag{1.1}$$

Using this, we commit to two calculations, first, we take the curl of this, and secondly, integrate after multiplying with velocity. Also, it is worth noting that to convert grad to k, we switch to the Fourier space in 1.3. Using this, we get:

$$\frac{\delta E}{\delta t} = 0 \implies E_2 = E_1 + E_3 \tag{1.2}$$

$$\nabla^2 E = \frac{\delta \omega}{\delta t} \implies k_2^2 E_2 = k_1^2 E_1 + k_3^2 E_3 \tag{1.3}$$

$$E_2 = E_1 + E_3 \tag{1.4}$$
$$k_2^2 E_2 = k_1^2 E_1 + k_3^2 E_3 \tag{1.5}$$
$$k_2^2 E_2 = k_1^2 (E_2 - E_3) + k_3^2 E_3 \tag{1.6}$$
$$k_2^2 E_2 = k_1^2 (E_1) + k_3^2 (E_2 - E_1) \tag{1.7}$$
$$E_3 = \frac{(k_2^2 - k_1^2) E_2}{k_3^2 - k_1^2} \tag{1.8}$$
$$E_1 = \frac{(k_2^2 - k_3^2) E_2}{k_1^2 - k_3^2} \tag{1.9}$$
$$\tag{1.10}$$

Therefore, when we say $k_3 \to \infty$, we can see that $E_1 = E_2$, which is called the inverse cascade. While in case $k_1 \to 0$, we see that $k_3 E_3 = k_2 E_2$, which is called the direct enstrophy cascade. These are shown in the figure 1.2. In this case, $k_1 < k_2 < k_3$.

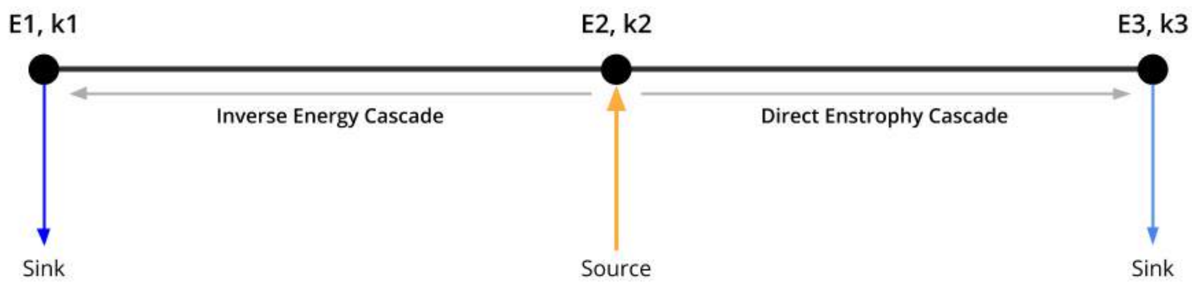

FIGURE 1.2: Energy Cascade in the Fourier Space

Further, other important things that help in reaching results for 2D turbulence are the fact that vorticity is a scalar, and therefore it is easy to quantify and interpret. Further, energy inside the domain is also an important quantifier, which we look at in greater detail.

1.3 About Taylor-Couette Flows

The motivation for this work came from the paper "Turublence Appearance and Nonappearance in Thin Fluid Layers" [4], which led to asking how a similar phenomenon would occur in a circular geometry, which was not very intuitive to begin with. The general idea was, however, to understand Taylor-Couette flows with a historical as well as physical perspective, and a few of those ideas have been written down here, to serve as an introduction to Taylor-Couette flows.

Taylor-Couette flows were initially used to measure the viscosity of fluids, and to study the stability of fluids inside cylinders. The setup essentially consists of two coaxial cylinders of different radii, and the fluid is filled between the two. One of these cylinders is then rotated and the setup is studied using various tools and means of measurement. Although demonstrably simple and trivial at the first glance, the flow proves to be extremely hard to explain reasonably, and has been the subject of active experimental, theoretical as well as numerical study for a very long time. This flow is still actively studied and a lot of unanswered questions till remain. The reason why Taylor-Couette flows are a good subject of study in circular geometries comes from the fact that they are well studied and have a lot of literature, but TC flows in 2D have not been studied well enough so far. To the best of our knowledge, there was no available literature dealing with turbulence in 2D TC flows, and we therefore concluded that not much has been done in this area of study for a very long time.

The analytical solution of the TC flows is described later in the section dedicated to the BCs and ICs, along with how the different ICs are imposed in our test case.

1.4 Computational Approach and Solver Selection

All the simulations were carried out using the Nek5000 Spectral Element Solver [1], made by the Argonne National Lab, and were run on XSEDE Comet systems at the San Diego Supercomputing Centre and the Wexac cluster at the Weizmann Institute. The solver was selected for the greater accuracy and stability of the spectral element method [6] compared to the finite element or finite volume methods. This solver is also known to be stable for long transient simulations, and itself does not contain very heavy modules. Adding to these inherent advantages is the fact that the solver is highly adaptable to the user input, and the "userchk" routine within the .usr file gives the user the ability to write his/her own parameters, and use those to output data either to the screen or redirect them to the file. This was essential to our work, and helped us get values of enstrophy as well as energy over time, which would have been a time taking process otherwise. The computational approach consisted of using the stream function to impose an initial perturbation on the flow over the laminar profile, at time $t = 0$, and then the 2D Navier-Stokes equation is solved continuously for all timesteps. The Spectral Element method is used for the spatial discretisation,and at this point it should also be made clear that this is different from the spectral method, in the way that the SEM uses piecewise polynomials of high degree to discretise, while the spectral methods use sines or cosines of high degree to achieve this. In the SEM, the solution and data are represented in terms of N th-order tensor-product polynomials within each of E deformable hexahedral (brick) elements. The SEM exhibits very little numerical dispersion and dissipation, which can be important, for example, in stability calculations, for long time integrations, and for high Reynolds number flows. [2]

The timestepping is taken care of by a second or third order BDFk/EXTk (Backward Difference or Extrapolation of order k) scheme, ie $k = 2, 3$. In our case, EXT3 is used for timestepping, ensuring third order accuracy in time throughout. The scheme can be generally descretized as:

$$\sum_{q=0}^{k} \beta_q \phi^{n-q} = -\sum_{p=1}^{k} \gamma_p c.\nabla\phi|_{t^{n-p}} + I^m \tag{1.11}$$

Where I^m = accounts for implicit contributions
β_q = Differentiation coefficients associated with the approximation of a derivative at time t^n based on known values at t^{n-q}
γ_p = interpolation coefficients
q = 0, 1, 2 . . . k
p = 1, 2, 3 . . . k

All the simulations that are conducted are pure DNS in nature, ie, directly solve the Navier-Stokes equation. Also, the maximum CFL number was restricted to 0.5. The simulations were checked for different mesh sizes, and these results are also checked for independence from the timestep. This can be read about in detail in the section 4

Apart from this, most of the post processing and data analysis was done with Visit and Paraview, and tools such as Gnuplot, MATLAB, LibreOffice etc were used to reach useful conclusions.

Chapter 2

Working and Mesh Details

2.1 Details of Cases

To begin work on the project and to gain familiarity with the Nek5000 platform, a trivial dimensional case was written, which just calculated torque on the walls as the user given parameter as part of the subroutine "Userchk". The specifics of the trivial case are given below:

This case was selected because the radii and angular velocities were both physically sensible, and the Courant number was taken to be low, so that the stability of the code and errors generated due to it are not big concerns in the very beginning.

Later, when the results of the trivial dimensional case were obtained, we made the switch to non-dimensional variables, and that made the entire problem independent of any dimensions whatsoever. The non-dimensional parameters were chosen as such, and the variables are given below:

Meaning	Symbol	Value	Unit
Radius (Inner)	R0	0.1	m
Radius (Outer)	R1	0.2	m
Angular Velocity (Inner)	w0	8.9e-03	rad/s
Angular Velocity (Outer)	w0	0	rad/s
Reynolds Number	Re	100	–
Density	ρ	1000	kgm^{-3}
Courant Number	Courant	0.9	–
Solver Parameters			
Number of Timesteps	NSTEPS	3000	–
Temporal Order	TORDER	3	–
Spatial Order	N	9	–
Absolute Tolerance	TOLABS	1e-6	–

Table 2.1: Details of the initial trivial case

Meaning	Symbol	Value	Unit
Radius (Inner)	R0	1	–
Radius (Outer)	R1	2	–
Angular Velocity (Inner)	w0	1	–
Angular Velocity (Outer)	w1	0	–
Reynolds Number	Re	100	–
Density	ρ	1	–
Courant Number	Courant	0.9	–
Solver Parameters			
Number of Timesteps	NSTEPS	3000	–
Temporal Order	TORDER	3	–
Spatial Order	N	9	–
Absolute Tolerance	TOLABS	1e-8	–

TABLE 2.2: Details of final non-dimensional case

At this point, it is also important to mention the non-dimensionalising variables which were used to get these parameters. They are:

$$R = \frac{R0}{R1 - R0}$$
$$w = \frac{w}{w0 - w1}$$
$$t = \frac{T}{2\pi(\omega0 + \omega1)}$$

2.2 Mesh Information

For the trivial cases, a smaller mesh was used in order to understand better the workings of the code, and an overall estimation of errors, along with shorter run times and lesser computational power at our disposal. The order of elements was, however, kept high enough, making the total number of elements in the mesh being equal to $8 \times 24 \times (9+1)^2 = 19200$ mesh elements (in a somewhat finite volume equivalent). The meshes were then further refined for runs upto Reynolds number 5000, and refined again after that. The mesh statistics are as follows:

Mesh for the trivial case:

- Elements in R: 8
- Elements in θ : 24
- Order of Spatial Elements: 9

Mesh for initial testing and production runs was of the configuration shown below, and had a total mesh count of $24 \times 320 \times (9+1)^2 = 768,000$ elements. This mesh was used to study the

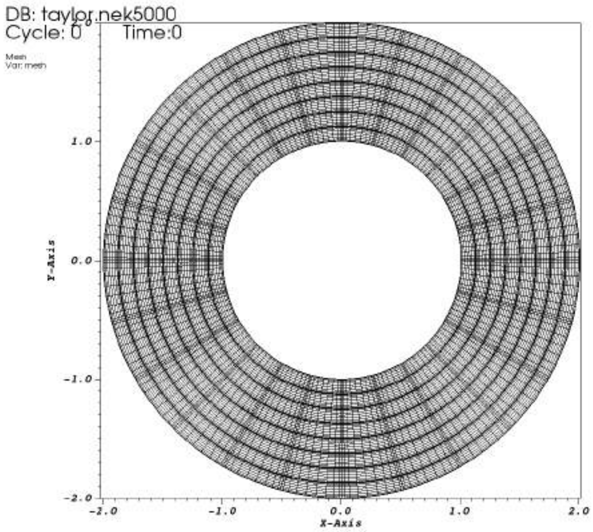

FIGURE 2.1: Case mesh for Trivial Cases

scaling and performance of the code on the Comet supercomputer, and also to introduce various test conditions:

- Elements in R: 24
- Elements in θ : 320
- Order of Spatial Elements: 9

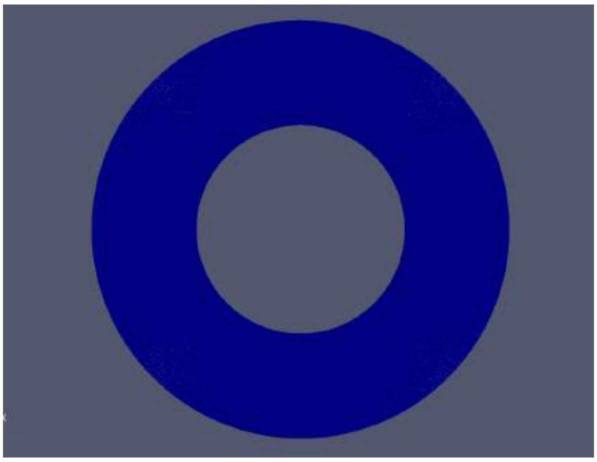

FIGURE 2.2: Case mesh for Initial Test and Production Runs

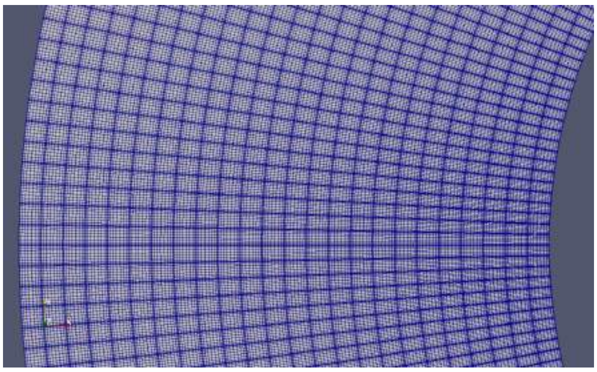

FIGURE 2.3: Close up of mesh for Intial Test and Production runs

For runs with Re = 10,000 or higher, a mesh of the following configuration is being used, with the toal mesh count being $72 \times 600 \times (9+1)^2 = 4,320,000$ elements:

Reynolds Number		100	500	1000	5k	10k
Mesh 1	Target ΔS	0.1096	0.0246	–	–	–
	Actual ΔS	0.0125	0.0125	–	–	–
Mesh 2	Target ΔS	–	0.0246	0.0129	0.0029	–
	Actual ΔS	–	0.0041	0.0041	0.0041	–
Mesh 3	Target ΔS	–	–	–	0.0029	0.0015
	Actual ΔS	–	–	–	0.0014	0.0014

Table 2.3: Mesh Data for various Reynolds' numbers

- Elements in R: 72
- Elements in θ : 600
- Order of Spatial Elements: 9

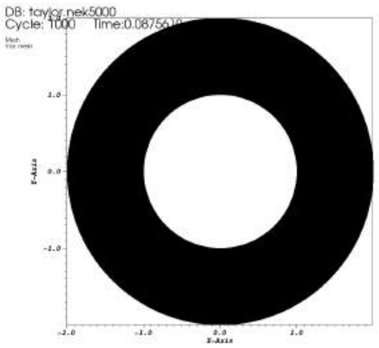

Figure 2.4: Case mesh for Mesh 3

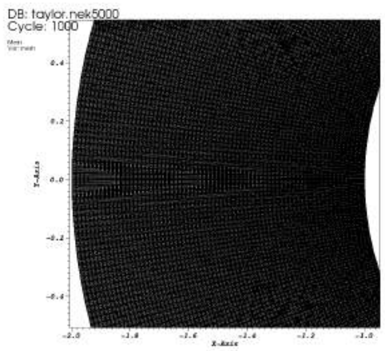

Figure 2.5: Closeup of Mesh 3

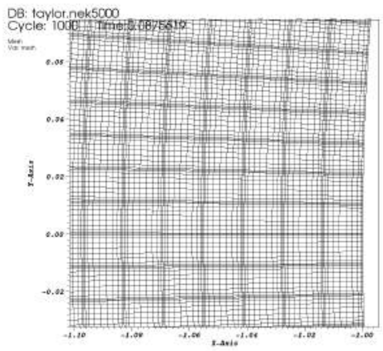

Figure 2.6: Closeup of Mesh 3 - 1.0 to 1.1 L

The non-dimensional first cell height (Y+) was selected as 0.9 for these meshes, and target ΔS is calculated using this. The data of the actual ΔS was picked from the cell data itself. Also, the data for all these meshes, which are being called Mesh 1, 2, and 3 for convenience, are as follows:

As it might be observed, The ΔS used for $Re = 5000$ is greater than 0.9 in Mesh 2, and therefore the mesh was updated to a greater number of elements. The same holds for the first mesh. Even for Mesh 2 at Re = 5000, the Y+ values are around 1.128.

Chapter 3

Taylor-Couette Flows - Boundary and Initial Conditions

3.1 Coordinate Transformations

Since the flow in this problem is inside a circular geometry, it makes sense to work in polar coordinates, which are a function of R and θ. Since the solver works in Cartesian, some coordinate transforms are important and need to be kept in mind while looking at the implementation. They are given as equations below:

$$V_x = \frac{dx}{dt} \qquad V_y = \frac{dy}{dt} \tag{3.1}$$
$$V_r = \frac{dr}{dt} \qquad V_\theta = \frac{d\theta}{dt} \tag{3.2}$$
$$X = Rcos\theta \qquad Y = Rsin\theta \tag{3.3}$$
$$R = \sqrt{X^2 + Y^2} \qquad \theta = tan^{-1}\Big(\frac{y}{x}\Big) \tag{3.4}$$
$$\tag{3.5}$$

Using these basic relations, the following can be written for V_x, V_y, V_r, V_θ

$$V_x = V_r sin\theta - RV_\theta sin\theta \tag{3.6}$$
$$V_x = V_r cos\theta - RV_\theta cos\theta \tag{3.7}$$
$$V_\theta = \frac{1}{2R}\Big(V_x sin\theta - V_y cos\theta\Big) \tag{3.8}$$
$$\tag{3.9}$$

$$V_r = V_x cos\theta + V_y sin\theta \tag{3.10}$$

3.2 Analytical Solution and Boundary Conditions

For the laminar solution of the Navier Stokes Equation in the Taylor-Couette flow geometry, the following results are obtained analytically:

$$V_\theta = Ar + \frac{B}{r} \tag{3.11}$$

$$V_r = 0 \tag{3.12}$$

where

$$A = \frac{\omega_1\Big(\omega_2 R_2^2 - \omega_1 R_1^2\Big)}{R_2^2 - R_1^2} \tag{3.13}$$

$$B = (R_1 R_2)^2 \Big(\frac{\omega_1 - \omega_2}{R_2^2 - R_1^2}\Big) \tag{3.14}$$

$$\tag{3.15}$$

When implementing no-slip and moving wall BCs, R0, R1, w0, w1 can be used to obtain A, B as constants, which are independent of the reference coordinate system. Further, as velocities are implemented in the cartesian coordinates, 3.6 - 3.10 can be used to convert these velocities to cartesian and implement.

The BCs are implemented in the following manner:

1. Use R0, R1, w0, w1 inputs to obtain A and B
2. Use a variable to store R as $x^2 + y^2$, then change R to sqrt(R), to make the variable R physically equal to radius
3. Define $cos\theta$ and $sin\theta$ as x/r and y/r
4. Convert V_θ and V_r to V_x and V_y
5. Use the initial BCs obtained from this (Resulting in no-slip walls) as the wall conditions

3.3 Define Initial Conditions

We considered two solutions, which are physical initial conditions, implying that the incompressibility condition along with the boundary conditions are satisfied throughout the domain. This problem has so far been worked on using two ICs, each of them enumerated below. As part of Nek5000, ICs are specified in the USERIC part of the .usr file, so the exact code for this implementation can be found in the source files. A small snippet of the ICs is also provided for reference. The three cases considered so far are:

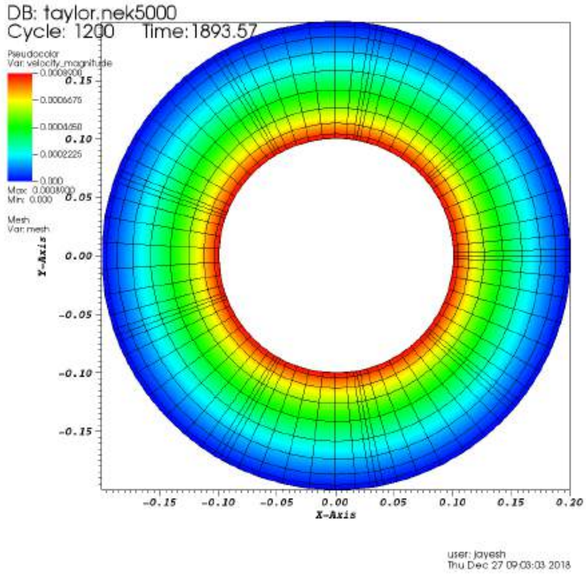

FIGURE 3.1: Analytical solution of Laminar Flow

1. Laminar profile as IC
2. Perturbation as IC, with laminar background to match the BC.

3.3.1 Laminar Profile

In order to implement the laminar profile as IC, in the USERIC subroutine, we used the variables "ue" as UX and "ve" as UY, and these would give the laminar solutions as ICs. The variables "ue" and "ve" correspond to the solutions obtained analytically using the method listed in the previous section.

The IC (velocity magnitude at t=0) is as shown in 3.2.

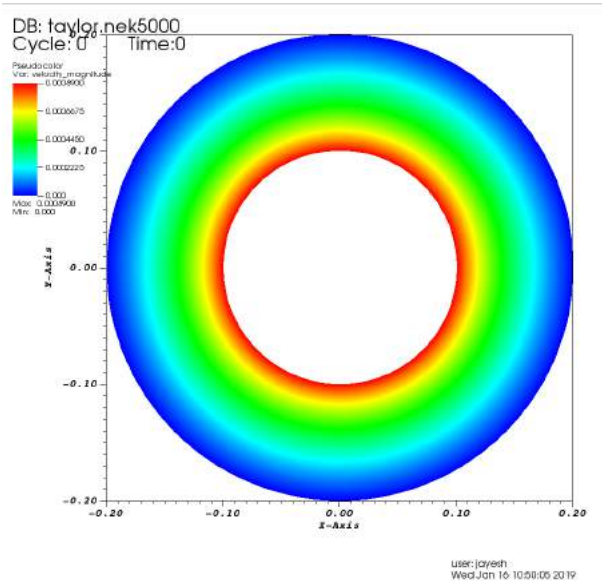

FIGURE 3.2: Laminar Flow profile as IC

3.3.2 Initial Perturbation IC

In order to introduce a perturbation as an IC which is physically feasible, it is important that the flow remains incompressible, and the Boundary Conditions are satisfied. This condition can be insured by making sure that:

$$\nabla \cdot V = 0 \tag{3.16}$$

$$V_{r0} = A(r0) + \frac{B}{(r0)} \tag{3.17}$$

$$V_{r1} = A(r1) + \frac{B}{(r1)} \tag{3.18}$$

$$\tag{3.19}$$

Introducing physically feasible perturbations can easily be done by simply using the stream function, as follows:

$$\Delta\phi = k(r - R_1)^2(r - R_2)^2 sin(m\theta) \tag{3.20}$$

This implies that the velocity of just the perturbation is given by:

$$v_\theta = -\frac{\delta\phi}{\delta r} \qquad rv_r = \frac{\delta\phi}{\delta r} \tag{3.21}$$

Simplifying this, we get v_θ and v_r as:

$$v_\theta = -2k sin(m\theta)(r - r0)(r - r1)(2r - (r0 + r1)) \tag{3.22}$$
$$rv_r = mk(r - r0)^2(r - r1)^2 cos(m\theta) \tag{3.23}$$

The divergence of this is given as:

$$\nabla \cdot V = \frac{1}{r}\left(\frac{\delta(rv_r)}{\delta r} + \frac{\delta v_\theta}{\delta \theta}\right) \tag{3.24}$$

Differentiating term by term, we get:

$$\frac{\delta(rv_r)}{\delta r} = 2(m)(k)(cos(m\theta))(r - r0)(r - r1)(2r - (r0 + r1)) \tag{3.25}$$

$$\frac{\delta v_\theta}{\delta \theta} = -2(k)(m)(cos(m\theta))(r - r0)(r - r1)(2r - (r0 + r1)) \tag{3.26}$$

Therefore, $\nabla \cdot V = 0$, proving that such perturbations always satisfy the incompressibility as well as the required BCs.

When these perturbations are inserted as ICs, $\phi + \delta\phi$ is given as input, and m and k are set arbitrarily. The amplitude of the perturbation increases or decreases by changing k, and m changes the frequency of the perturbation. As part of the code, for m=1, the implementation is as given in the snippet below:

```
m = param(113)                                  C Set at 1 in *.rea
ep = param(114)                                 C Set at 10 in *.rea
K = param(115)                                  C Set at 1/0 in *.rea

e  = gllel(eg)
y = ym1(i,j,k,e)
x = xm1(i,j,k,e)
r = (x*x)+(y*y)
r = sqrt(r)
th = atan2(y,x)
zx = m*th
sth = sin(zx)
cth = cos(zx)
vth = -2*ep*sth*(r-r0)*(r-r1)*(2*r - r0 - r1)
vr = (m*ep*(r-r0)*(r-r0)*(r-r1)*(r-r1)*cth)
vr = vr/r
ux = vr*cth - r*vth*sth + K*ue(i,j,k,e)
uy = vr*sth + r*vth*cth + K*ve(i,j,k,e)
uz = 0
temp=0
```

where xm1 and ym1 are the transformed coordinates (Polar coordinates) and when m=1, $sin\theta = y/r$ and $cos\theta = x/r$.

The perturbations when introduced this way result in the profile shown in 3.3. Also, when the laminar profile (as set in 3.3.1) is added, ie $k = 1$, the profile obtained as the IC is as given in

3.4. Although another point which should be noted here is that in figure 3.3, the IC does not satisfy the BCs, and therefore a laminar background must be introduced. When the laminar background is introduced, for small aplitudes of the perturbation the case looks like figure 3.4, and looks like 3.3 again for larger values of amplitude, although it still satisfies the BCs.

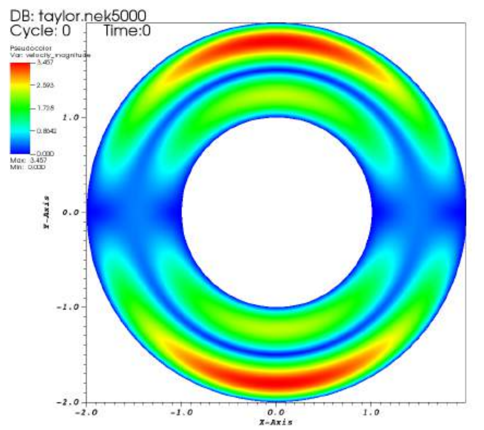

FIGURE 3.3: Only perturbation

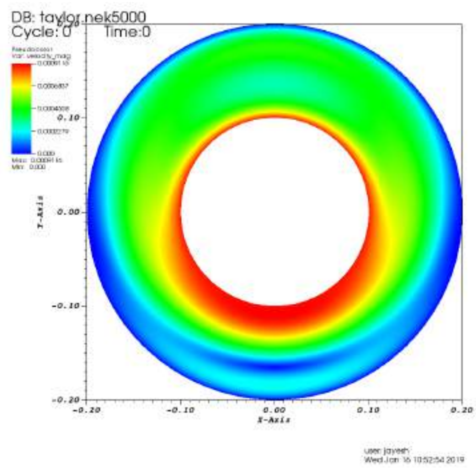

FIGURE 3.4: Perturbation with Laminar Background

3.4 Implementing Total Energy, Vorticity, Wall Shear and Enstrophy

3.4.1 Definition

While velocity itself gives a large picture, in terms of analysis and post processing, the dataset is incomplete until interpreted with vorticity, energy and enstrophy, and since it is a Taylor-Couette flow, wall shear as well. These are essential in analysing not only the stability and progress to laminar flow, but also play an essential role in estimating errors within the flow itself.

Each of these parameters needs a definition, since the same has not been made before. Therefore the definitions follow:

- Energy: Total energy across the domain is useful in checking how the solution has progressed to laminar flow. It is given by:

$$E = \int\int \frac{v^2}{2} r\, dr\, d\theta \tag{3.27}$$

- Enstrophy: This is used to quantify the dissipiation in the fluids. Enstrophy is useful in transient turbulent flows. Given by:

$$\epsilon = \oint_S |\nabla \times \vec{u}|^2\, dS \tag{3.28}$$

- Vorticity: This is the curl of the velocity vector, and gives the local spinning motion of a fluid within the domain. It is given by:

$$\vec{\omega} = \nabla \times \vec{u} \tag{3.29}$$

3.4.2 Implementation

These are initialised as zeros in the beginning, and are then implemented as part of the code using the code listing. the variables vvx and vvy are given one value for each mesh point iteratively, and the variables areasum, enersum, enstsum and vortsum are calculated using these. Vorticity was previously calculated using the script "vort3", which writes vorticity as part of another file before this part of the code. The output are the variables that give the total area, energy, enstrophy and vorticity.

The code for the loops and implementation are below:

```
do e=1,nelv
      do j=1,ly1
      do i=1,lx1
         weight =  bm1(i,j,1,e)
         vvx = vx(i,j,1,e)
         vvy = vy(i,j,1,e)
         areasum = areasum + weight
         enersum = enersum + 0.5 * (vvx*vvx + vvy*vvy) * weight
         enstsum = enstsum + vort(i,j,1,e,1)*vort(i,j,1,e,1) * weight
         vortsum = vortsum + vort(i,j,1,e,1) * weight
      enddo
      enddo
      enddo
```

Once averaging was setup for space as well as overall quantities could be written, the only parameter left to analyse was the code performance, with both, smaller as well as larger meshes. Since the work so far only concerns Re = 10000 as the maximum, handling and performance of the code was only tested for meshes 1 and 2, as described in the section ??. The code was also tested for larger meshes to handle Re = 20,000, and the results are similar to the other meshes.

Chapter 4

Code Performance

4.1 Methodology

Since the code had to be tested for its parallel processing capabilities, and the performance of the supercomputers themselves had to be proven before more serious production level runs could be executed, the scaling and parallel processing capabilities were analysed, and strong scaling tests were carried out, by changing both, number of cores for the same case, and the number of collocation points while running on the same number of cores. The speedup and change in number of collocation points were analysed in great detail, the results of which are shared in the next section.

Another problem we encountered was non-uniform runtimes on the same case, and that was also later resolved. The results of all these runs are listed in the next section. The errors produced by the code that cause deviation from anaytical results are also analysed, and these have also been listed in the section after the code performance. The errors are estimated using divergence and the value of radial velocity at laminar flow, and more details about the same are listed later.

4.2 Scaling

4.2.1 Strong Scaling on the same case

The details of the first case are:

- Mesh Size: 320x24
- Number of collocation points: 7
- FVM mesh equivalent: $320 \times 24 \times (7+1)^2 = 491,520$ elements
- Run time: 0.099 seconds

- Δ T: 1E-04 s
- Number of cores tested: 1, 2, 4, 8, 24, 48, 96, 128

The timestep was fixed such that the Courant Number stayed below 0.5 (the stability criteria of the code after extensive testing) and went as low as 0.133 towards the last time step. The case was run for a fixed 1000 timesteps, and strong scaling was specifically studied, since the geometry was fixed and only the initial energy (and velocity) was changing, so strong scaling was the most relevant to the study. The results of the scaling study are as tabulated below:

Parameters	1	2	4	8	24	48	96	192
Total time (s)	3.11E+02	1.52E+02	7.86E+01	4.07E+01	1.94E+01	1.32E+01	1.12E+01	1.43E+01
Total time w/o IO (s)	3.09E+02	1.51E+02	7.77E+01	3.99E+01	1.86E+01	1.18E+01	8.92E+00	1.04E+01
time/timestep (s)	3.09E-01	1.51E-01	7.77E-02	3.99E-02	1.86E-02	1.18E-02	8.92E-03	1.04E-02
avg throughput/timestep	6.14E+05	6.29E+05	6.10E+05	5.95E+05	4.25E+05	3.35E+05	2.22E+05	1.01E+05
Max memory usage (GB)	5.31E-01	9.87E-01	1.90E+00	3.72E+00	1.10E+01	2.39E+01	4.82E+01	9.79E+01

TABLE 4.1: Scaling and times vs number of cores

The same performance, with respect to ideal scaleups are as given in the graph shown.

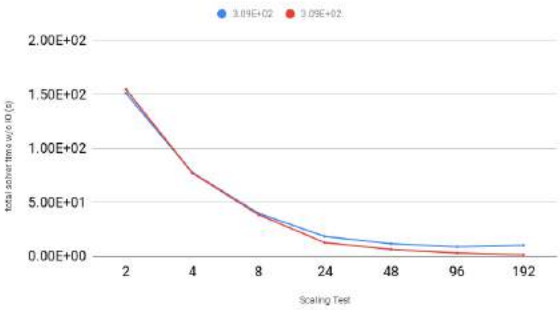

FIGURE 4.1: Case mesh for Trivial Cases

An interesting observation here is that the runtime decreases, albeit non-linearly, upto 96 cores, after which it begins to increase. This occurs due to the number of mesh elements per core becoming so small that more time is spent communicating between cores than is spent in computation in the respective cores. This also implies that the idle times of the cores is larger, and efficiency is lost. When we look at the solver time, we can also see that for 4 nodes (96 cores), we still use up around (96×8.92) 856.32 solver seconds, which is at (48×11.8) 566.4 solver seconds for 2 cores. This implies that for smaller cases (<8000 Spectral elements), we can say that efficiency is retained only upto two nodes, and therefore only two nodes were used for computation.

Benchmarking of Mesh 3, being used at Re = 10k and higher have been omitted since they present no new information on the solver statistics.

4.2.2 Scaling by change in collocation points

While increasing the collocation points, the effective number of mesh points as well as the accuracy of the solver are being increased, which in turn increases the runtime and comparable RAM usage. Since the previous case had already run on all processors using N=7, this case was run on the second most optimal option, using 96 cores (or 4 Nodes) for the study. The details of the study remain same as the previous, and are as given below:

- Mesh Size: 320x24
- Number of collocation points tested: 6,7,8,9,10
- FVM mesh equivalent: $320 \times 24 \times (n + 1)^2$ = 376,320; 491,520; 622,080; 768,000; 929,280 elements
- Run time: 0.099 seconds
- Δ T: 1E-04 s
- Number of cores:96

The results of these runs are as given in the table below:

Parameters	6	7	8	9	10
Total time (s)	8.204	11.21	14.98	16.92	17.094
Total time w/o IO (s)	7.207	8.92	12.42	14.11	13.899
time/timestep (s)	0.0072	0.00892	0.0124	0.01411	0.01389
avg throughput/timestep	2.018E+05	2.21E+05	2.077E+05	2.31E+05	2.347E+05
Max memory usage (GB)	36.93	48.24	53.88	58.919	58.929
FVM Mesh Equivalent	376320	491520	622080	768000	929280

Table 4.2: Scaling and times vs number of collocation points

4.2.3 Inferences

Inferences drawn from this can be that for N=6, the system used an extremely low amount of RAM, and also had the lowest run time, after which the increase in runtime was almost linear, except between N=9 and N=10, where the jump of almost 0.1s can be considered negligible. Also, the increase in the number of mesh elements, which is around 2.5× between N = 10 and N = 6, and the increase in run time, which is approximately 2.03× makes it clear that the tradeoff to increase the number of collocation points instead of mesh elements is a worthwhile one. The Nek5000 documentation also suggests the same as our findings. However, one last problem which was to be looked at remained, and that is the scaling across the same case for different independent runs.

4.3 Independent Runs and Runtime Issues

We noticed that for the same case, and for N=6, the runtimes using the previous settings (GNU Compliers) were inconsistent, and there were large changes in runtime for the same physical case. In order to find the cause of this and fix this problem, we decided to run a series of independent runs, and change one thing at a time and see the results for ourselves. For the various independent runs, we used the case which was the largest among the ones above, and used a single node. The details of the same are given below:

- Mesh Size: 320x24
- Number of collocation points: 10
- FVM mesh equivalent: $320 \times 24 \times (6 + 1)^2 = 376,320$ elements
- Run time: 0.099 seconds
- Δ T: 1E-04 s
- Number of cores: 24

For this run, the case files were copied as folder 01 through 05, and the test case was run. Previously, we had been encountering problems, which were solved by using the scratch space instead of the home folder, and running using the latest Intel compilers rather than the previously used GNU compilers. These two changes made the run-time reliable enough, and the results of these independent runs are as shown in the table below:

Parameters	01	02	03	04	05
Total time (s)	84.95	86.439	86.69	85.738	87.22
Total time w/o IO (s)	84.30	85.69	86.080	85.046	86.563
time/timestep (s)	0.0843	0.0856	0.0860	0.0850	0.0865
avg throughput/timestep	3.088E+05	3.038E+05	3.025E+05	3.061E+05	3.008E+05
Max memory usage (GB)	14.801	14.801	14.801	14.801	14.801

Table 4.3: Scaling and times vs number of collocation points

The same run done multiple times also shows that the code is robust enough and does not deviate from the solution even when run multiple times. The solver and computational errors are also small enough to not cause major deviation, which helps build greater trust in the code. Based on these scaling runs, a few conclusions were drawn for Mesh 2, which are listed below in the conclusions section. More detailed data of individual timesteps with the laminar background on and off for the first thousand steps is presented in Figures 4.2 and 4.3. This shows that with the laminar background turned on, the mesh is able to handle the initial conditions much better, since the IC has a much smaller gradient, while with the laminar background turned off the the sharp gradients increase the time of the solutions. The times with the laminar background switched off were 82.9, 83.5, 83.8, 93.2 and 83.7s respectively for all these runs, and the memory usage was the same. Average lower runtimes of the laminar background turned off can also be explained by a lesser initial energy.

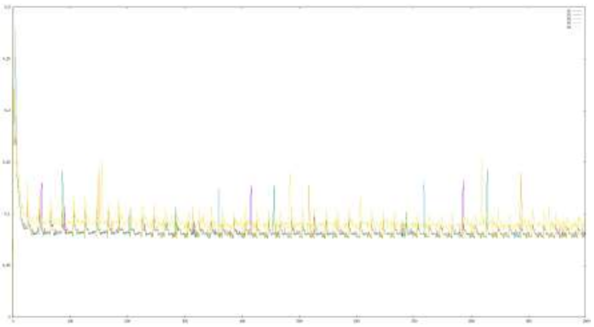

Figure 4.2: Time per timestep for independent runs with Laminar background On

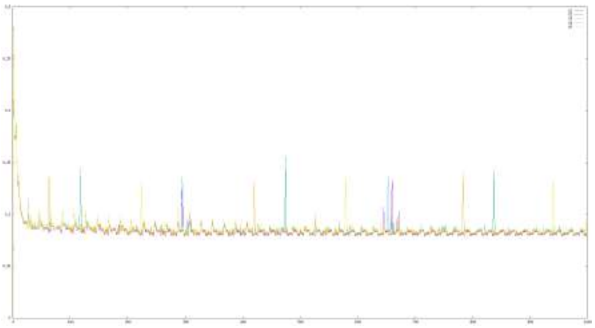

Figure 4.3: Time per timestep for independent runs with Laminar background off

4.4 Scaling: Conclusion

From these scaling results, we see that for Mesh 2, the code runs optimally for 2 nodes, and retains efficiency upto 4 nodes, so all cases were run on either 2 or 3 nodes to begin with. When larger meshes are used, the number of usable nodes can be expected to go up, as the Nek5000 documentation suggests it stays efficient until 20,000 elements per node, and is extremely scalable from 2000 elements. The code is also found to be reliable enough to run huge cases, and there were no apparent drawbacks. The cases run so far seem to be grid independent, which was not explictly tested, but the results were compared to analytical results for reference. The comparison between Mesh 1 and Mesh 2 and analytical results is presented in the Figures 4.4 and 4.5, which was compared to the laminar solution after it was attained. This was done at Re = 1000 due to restrict use of computational power, but will later be checked for Re = 10k for consistency.

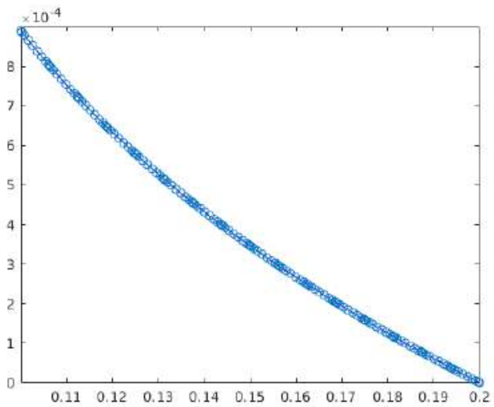

Figure 4.4: For Fine Mesh

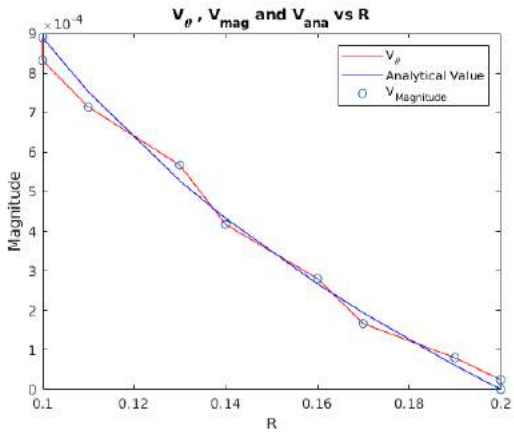

Figure 4.5: For Coarse Mesh

4.5 Error Estimation

The code also was tested for errors using a few test cases, the smaller meshes (Mesh 1 and Mesh 2) were both analysed for errors, and for this the results obtained by the solver (Processed using paraview) were compared to the analytical results. Since the problem at hand is one of incompressible flow in which the velocity in the radial direction is zero, both these analytical results can be used to quantify the errors on the grid, and the results of these should ideally be less than the solver tolerance, which is set at 1E-08. To formalise this argument, the following can be said:

$$\nabla \cdot V < 10^{-8} \tag{4.1}$$

$$V_x \cos\theta + V_y \sin\theta < 10^{-8} \tag{4.2}$$

The images as shown in Figure 4.6 and 4.7 show the divergence on the grid normalised to solver tolerance. The absolute value of these tolerances are of the order of E-12, which is less than the solver error. This therefore shows that the simulation matches the physical settings that have been given, and can be assumed to be correct to a large extent.

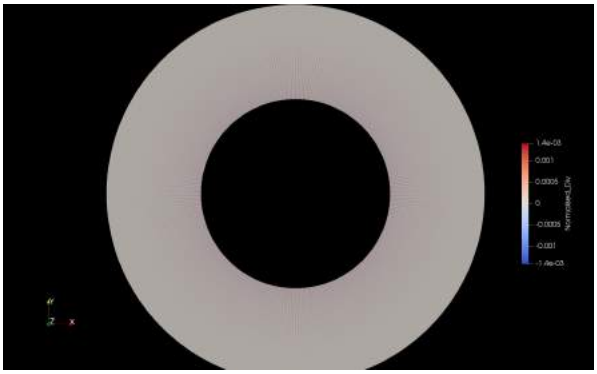

FIGURE 4.6: Normalised Errors on Mesh 2

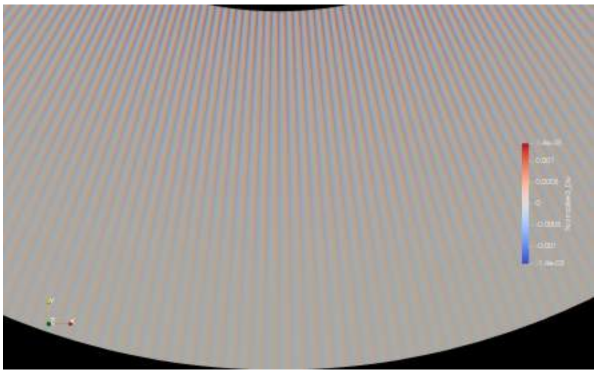

FIGURE 4.7: Normalised Errors on Mesh 2 (close-up)

Further, the comparison for V_r was made on the smaller mesh (Mesh 1) and that is shown in Figures 4.10 and 4.11. Figure 4.11 shows the divergence at the beginning of the simulation, with the perturbation at the maximum aplitude.

4.6 Errors: Conclusions

Looking at the errors throughout on the grid, the problem seems to be physically correct and the mesh is able to sustain the given problem physics, and for larger meshes the non-dimensional first cell height is to be adjusted and the problem tends to be mesh independent. The meshes thus used are also using higher order accuracy using a large number of collocation points, and a

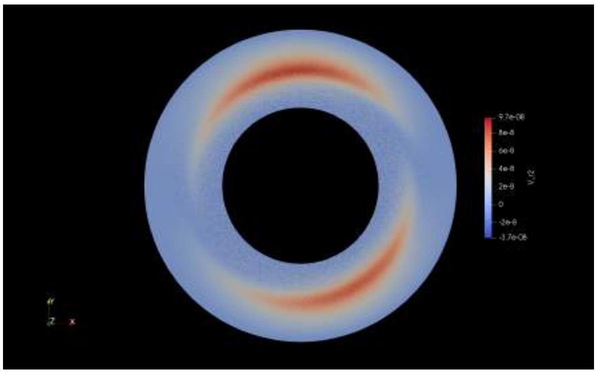

FIGURE 4.8: Magnitude of V_r on Mesh 2

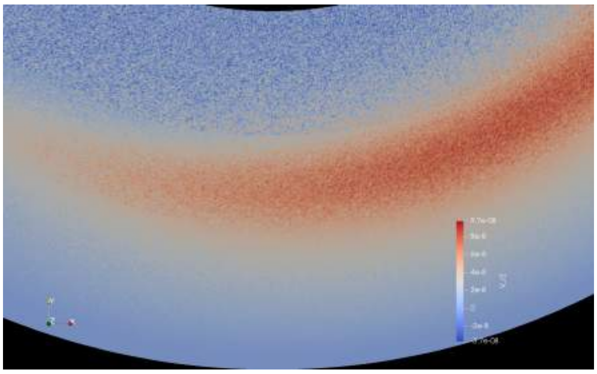

FIGURE 4.9: Magnitude of V_r on Mesh 2, Close-up

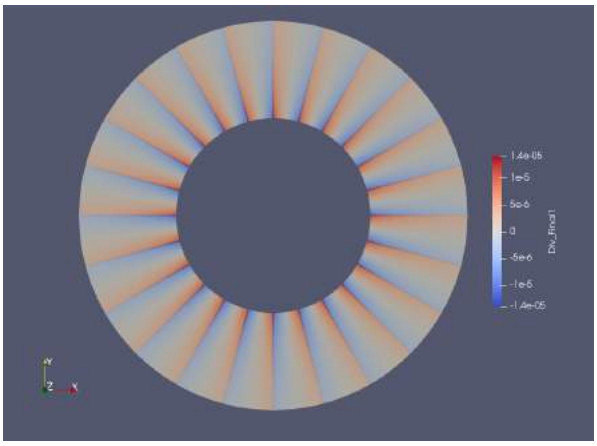

FIGURE 4.10: Normalised Errors on Mesh 1, Laminar Profile

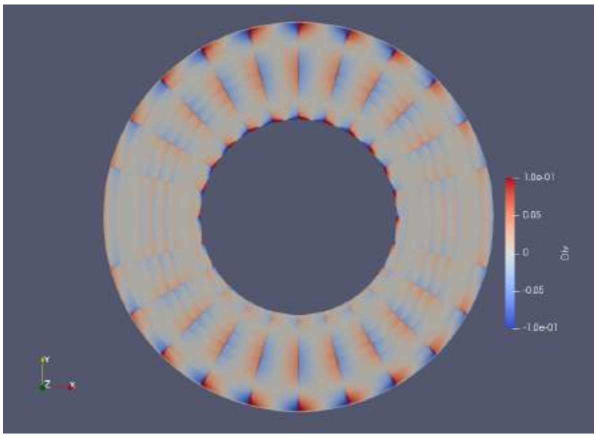

FIGURE 4.11: Normalised Errors on Mesh 1, Perturbation Energy

third order in time is used. Therefore, the results can be relied upon before Re = 10000, and right after that Mesh 3 promises to deliver reasonably good results.

Chapter 5

Results and Discussion

5.1 Visualising Perturbations

In order to understand how the cases are proceeding, it is first important to visualise how the various perturbations are implemented on the grid. The perturbations are as shown in 3, more specifically in Equation 3.22. Perturbations created by changing the various values of m and k are as given below:

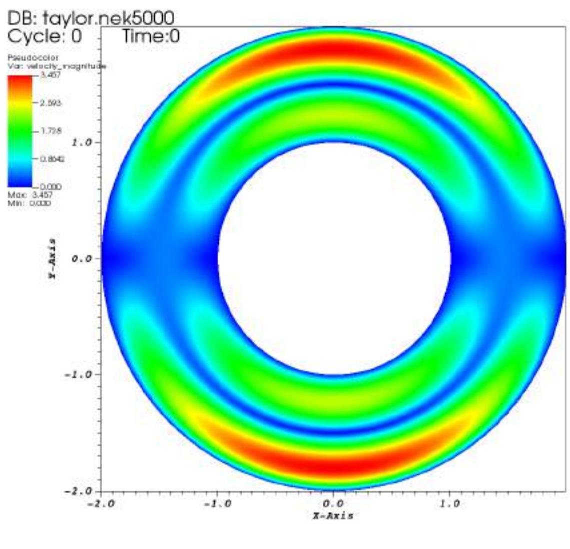

FIGURE 5.1: Initial Perturbation; $k = 10$ and $m = 1$

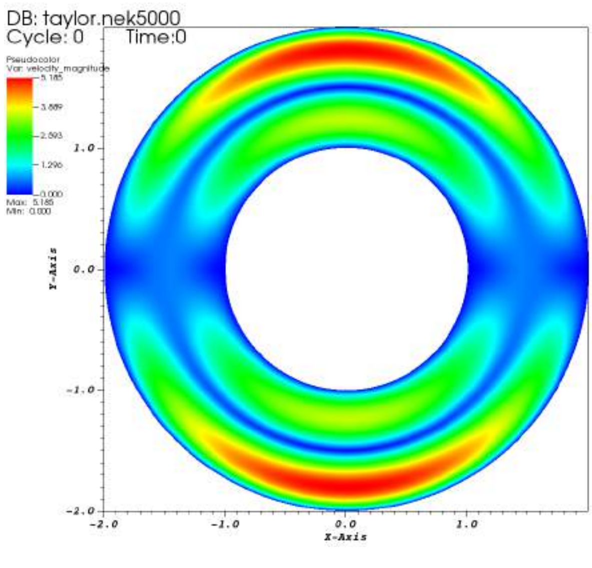

FIGURE 5.2: Initial Perturbation; $k = 15$ and $m = 1$

This makes it amply clear that the variable k changes the amplitude of the perturbation, while changing m changes the number of modes (or frequency) of the perturbation. In studying the results so far, k is varied while m is kept constant. The solution with this condition is allowed to evolve in time, and the results are observed.

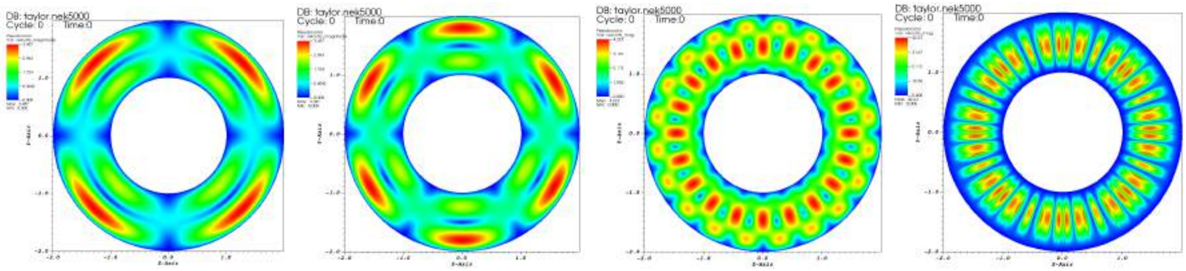

(A) $k = 10$ and $m = 2$ (B) $k = 10$ and $m = 3$ (C) $k = 10$ and $m = 10$ (D) $k = 10$ and $m = 100$

FIGURE 5.3: Change in IC by changing parameter 'm'

5.2 At Reynolds' Number 1,000

5.2.1 Initial Energy 3.862

When the case is run using Re = 1000 and allowed to evolve with time, The case was run with $K = 5$ and $K = 10$, Energy is scaled non-dimensionally to Laminar energy, which is 0.99152 J, The energy for $K = 5$ is 3.86 and 12.158 respectively, and since energy is dependent on velocity only, the initial energy is independent of Re.

At $Re = 1000$, and using $K = 5$, the evolution proceeds as shown in the Figures 5.4a to 5.4h and the vorticity during the evolution is shown in 5.5a to 5.5h.

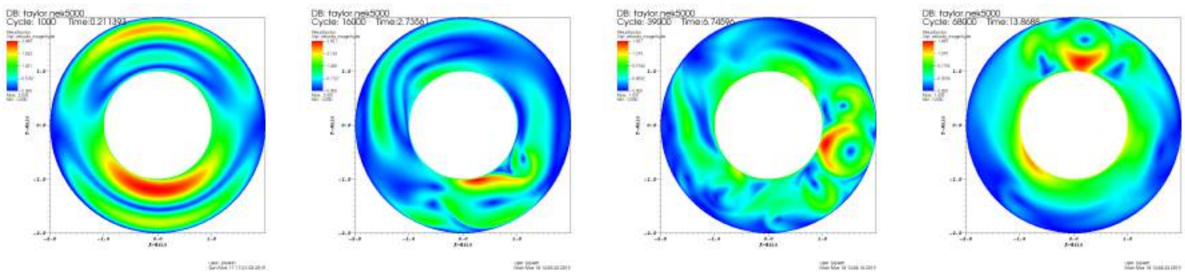

(A) $t = 0.21$ s (B) $t = 2.73$s (C) $t = 6.74$ s (D) $t = 13.86$ s

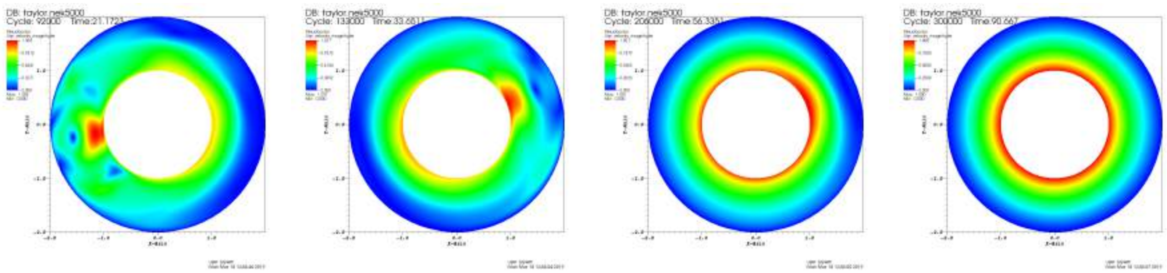

(E) t=21.17s (F) t=33.65s (G) t=56.33s (H) t=90.667s

FIGURE 5.4: Velocity profile at various times at $Re = 1000$, $k = 5$

On close inspection of the evolution in time, it can be seen that the initial condition first breaks left and right symmetry, which is due to the rotation of the inner ring (which is rotating in the anticlockwise fashion), and the upper and lower symmetry is also quickly broken. After that, the lower end generates a large vortex which continues for a very long time in the evolution (Upto

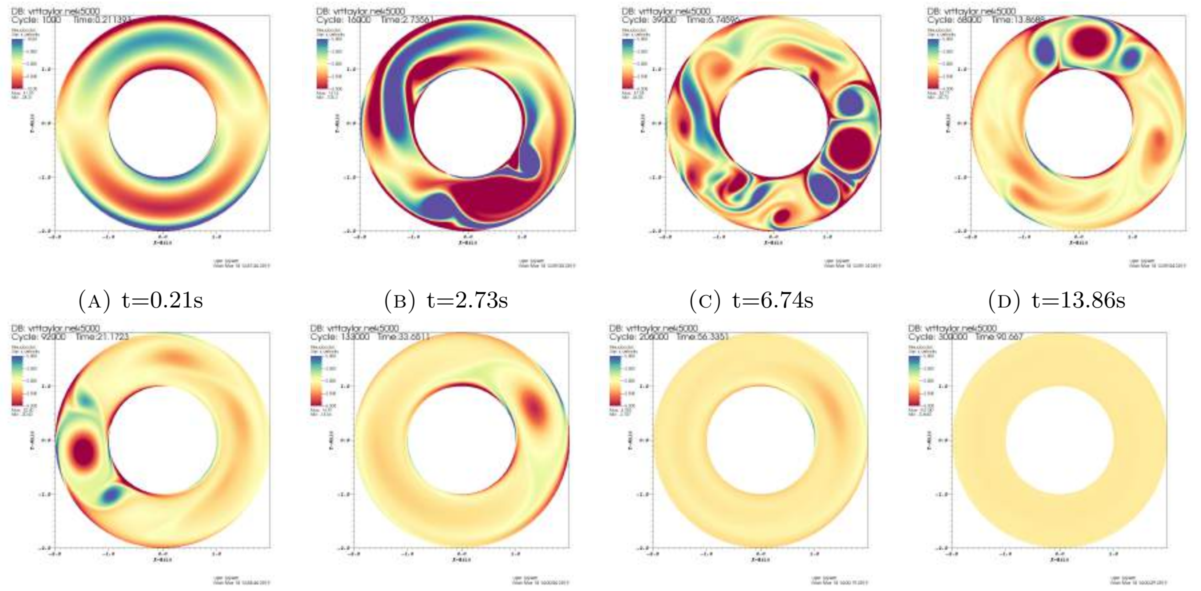

(A) t=0.21s (B) t=2.73s (C) t=6.74s (D) t=13.86s

(E) t=21.17s (F) t=33.65s (G) t=56.33s (H) t=90.667s

FIGURE 5.5: Vorticity profile at various times at $Re = 1000$, $k = 5$

83s). The cyclone-anticyclone symmetry is seen at around 5s, in which the primary vortex is an anti-cylcone, while it has two symmetric cylones on either side. These vortices lose energy in the same fashion for a very long time, and at around 13.86s, only these vortices are prominent enough to be noticable. The presence of very obvious vortex streaks can also be seen, which are counter-rotating in the opposite side of the vortex, and are present on both, the inner as well as outer rings. Further, the vortices can be losing energy upto 21s, right before which the symmetry between the two cyclones is lost. As the vortices keep losing energy, at 33s it can be seen that the central vortex has also lost a majority of its energy, and the vortex streaks are the only observable characteristics of the stage.

Now, around 56s, the vortex has almost disappeared and the vortex streaks are present. This stage right after this becomes even more interesting, as it is the lowest energy state in the case. As the case keeps on evolving, the vorticity reaches that of the laminar flow, and the normalised vorticity reaches zero. The stage at 90s is around 95% laminar energy, and therefore some vorticity can still be seen.

The most interesting conclusion here comes in the form of total energy of the system, the details of which are still not fully understood. The total energy of the system analytically at laminar flow is 0.99152 J, and all energy values written after this are normalised with respect to this energy, until the unit is specified. The minimum energy of this evolution is 0.9733, which is 2.7% less than the laminar energy. Also, this minimun occurs at 76 s, which is 50 s before 98% laminar energy is detected. The rate of decrease of energy over time is as shown in Figure 5.6.

The energy after reaching the minimum begins increasing back to laminar energy. This observation was puzzling to us, and therefore we wanted to see if this could be replicated with other Reynolds' numbers.

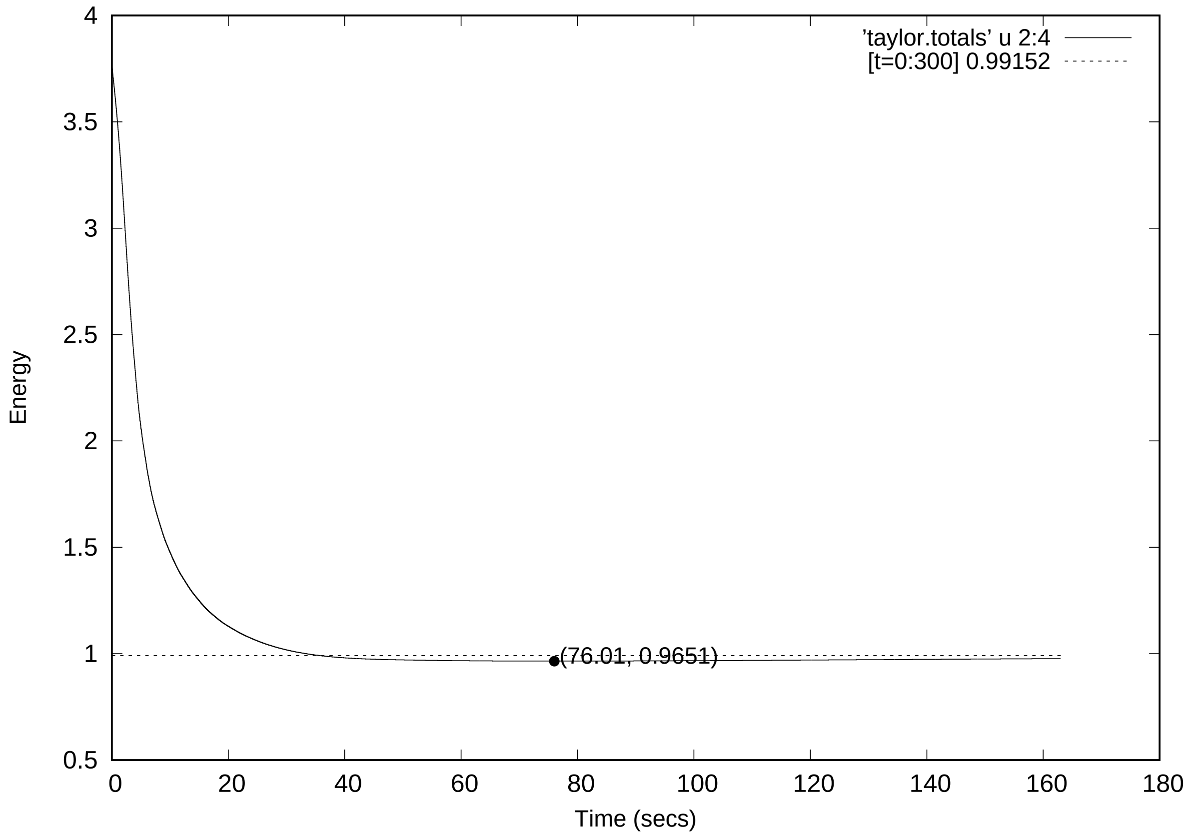

FIGURE 5.6: Energy inside the domain, $Re = 1000$ $k = 5$

5.2.2 Initial Energy 12.158

When the initial energy is increased by increasing the aplitude, K upto 10, it gives a non-dimensional energy of 12.158, which is about 3.22 times as much as the one in the previous case. The evolution of that proceeds can best be understood using a vorticity plot, and therefore velocity is not included until necessary, and the difference in plots between velocity and vorticity can be spotted by looking at the colors of the plots, where the red to blue is for vorticity, while those including greens and yellows belongs to velocity. The plots at $K = 10$ ($IE = 12.178$) are shown in Figures 5.7a to 5.7l.

When looking at the vorticity plots, a few interesting conclusions can be drawn. Initially when the symmetry is broken, three anticyclone vortices are formed which are surrounded by cyclones. The vorticity and therefore the energy quickly decrease, and by 9.125s the vorticity has decreased enough. At this point, five anticylones can be seen with cyclones spread intermittently between them. This stage is shown in figure 5.7b. This stage then evolves to where one anticyclone vortex has disappeared, and four vortices can be seen. What is prominent here is that the vortex streaks next to the vortices are in the opposite direction, in both cyclone and anticyclones, and they take energy from these streaks and get weaker. The vortex streaks on either side are in the same direction (negative vorticity), which is opposite to the direction of rotation of the ring. this stage is shown more clearly in figure 5.7c. At around 17s, one of the vortex is about to die, and the cyclones look much weaker than the given profile.

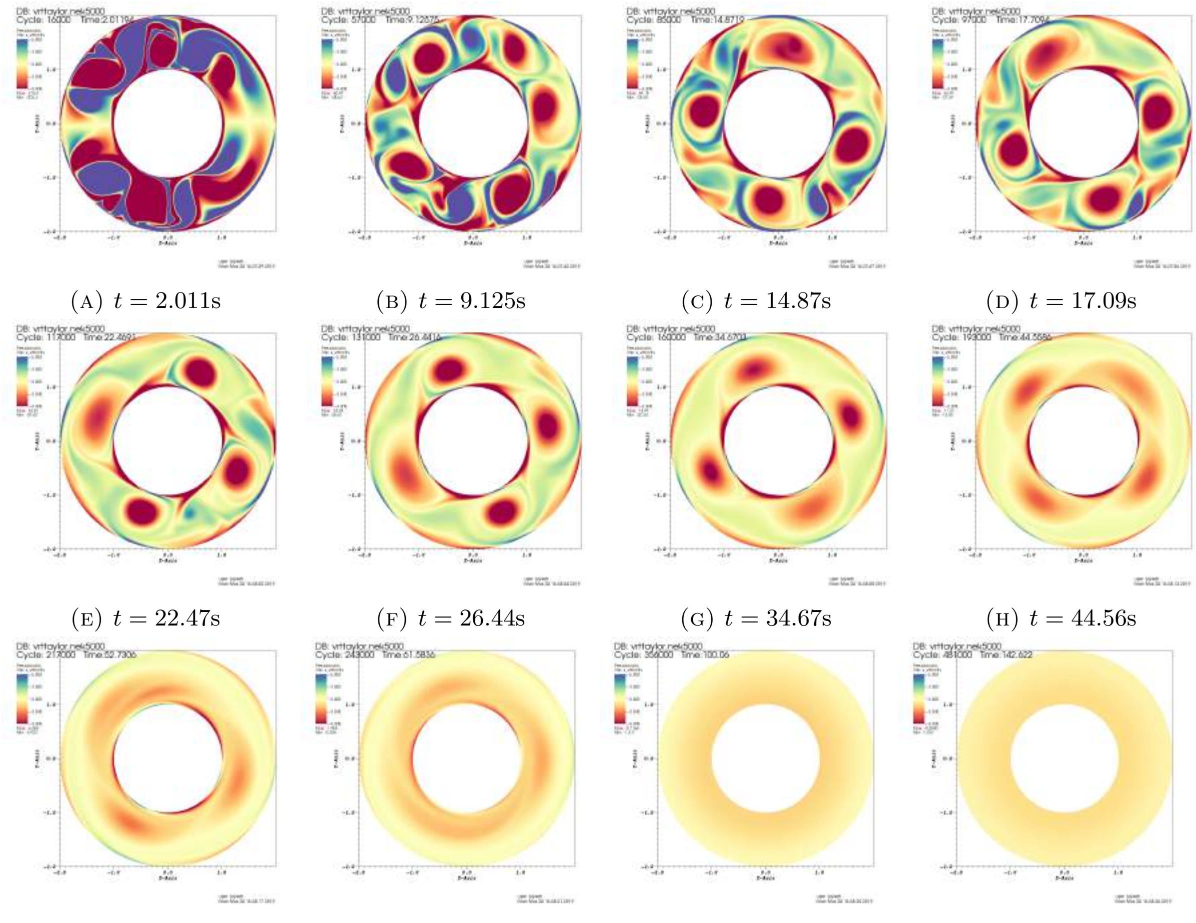

(A) $t = 2.011$s (B) $t = 9.125$s (C) $t = 14.87$s (D) $t = 17.09$s

(E) $t = 22.47$s (F) $t = 26.44$s (G) $t = 34.67$s (H) $t = 44.56$s

(I) $t = 52.73$s (J) $t = 61.58$s (K) $t = 100.06$s (L) $t = 142.62$s

FIGURE 5.7: Vorticity profile at various times at $Re = 1000$, $k = 10$

As time progresses, the vortices can be seen to get even weaker, as they continue to rotate with the inner ring. The vortex streaks also get weaker, and the observations about the vorticity can be seen seen even till a much later time, upto 53 seconds, as seen in figures 5.7d to 5.7i. In figure 5.7i, it is clear that one of the vortex has died down and the vortex streaks are also much weaker by now. A while later, at around 100 seconds, the energy has died down and the vorticity can be seen approaching the laminar viscosity. After 55.66s, energy increases until the system reaches the laminar value, and the rate of this increase keeps on decreasing as the velocity approaches 76% laminar energy. This is the last stage of the evolution and is shown in figure 5.7l.

Referring to 5.8 shows us the evolution of energy in the domain, which decreases continuously to reach 0.5867 non-dimnesional units, which is achieved at 55.66s (or 8.85 revolutions of the inner ring). After this, the energy slowly increases to the laminar state. The solution reaches 76.85% of laminar energy at 142.94s, or 22.74 revolutions of the inner ring, after which it is stopped. The rate of increase of the solution to laminar state is rather slow after this state, which is that calculation is avoided in the interest of computational time. Connecting this to the previous previous results, we see that the minimum energy is less than the laminar energy here as well, and that based on the energy, the minimum energy is inversely related to the initial energy.

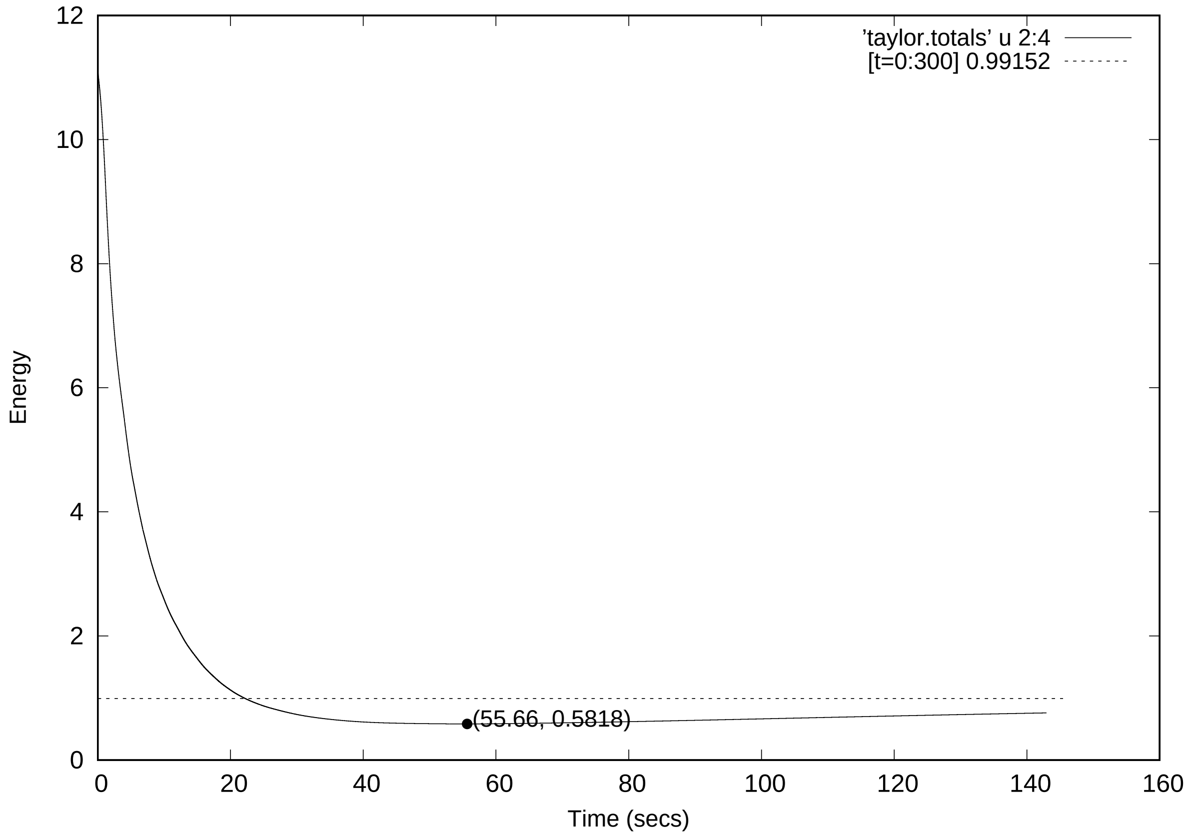

FIGURE 5.8: Energy inside the domain, $Re = 1000$ $k = 10$

5.3 At Reynolds' Number 3,000

5.3.1 Initial Energy 3.862

When Figure 5.9 is seen, we can see what happens in case of Reynolds' number of 3000, which is also very similar to $Re = 1000$. Initially, the lower end of the ring generates a big anticylcone vortex, which propagates throughout the domain. Although one characteristic which is different here from Re = 1000 is that some more vortices are generated, and one of the cyclone satellite vortex loses energy much faster than the other, which is made clearer by Figure 5.9b, which shows the cyclone vortex next to the anticyclone near the Y axis losing energy faster than the other vortex, which is right of the anticylcone. This vortex loses energy very rapidly and disappears, as can be seen in figure 5.9c and figure 5.9d.

As the case evolves in time, it can be seen from figure 5.9f that only one prominent vortex remains, which is in the anticyclone direction. With time, this vortex rotates within the ring and keeps on losing energy, until the vortices are extremely faint and the vortex streaks remain prominent. Since there are no prominent cyclone vortices, the two anticylcones keep chasing each other and losing energy in time, as can be clearly seen in the differences between 5.9h and 5.9k. The vortex streaks are still present in the given case upto this time, after which they begin to disappear.

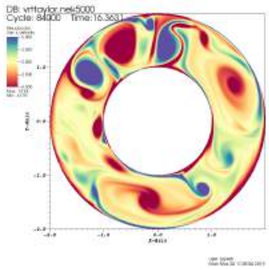

(A) $t = 16.36$ s

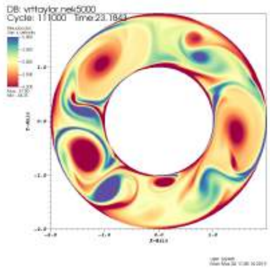

(B) $t = 23.18$ s

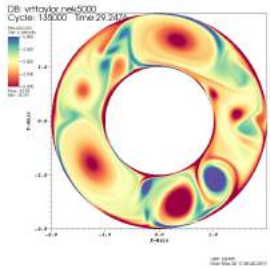

(C) $t = 29.24$ s

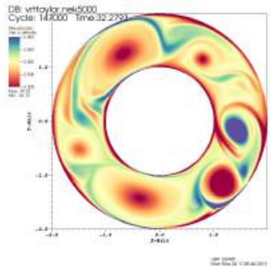

(D) $t = 32.28$ s

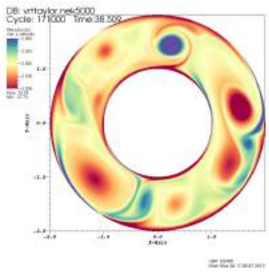

(E) $t = 38.50$ s

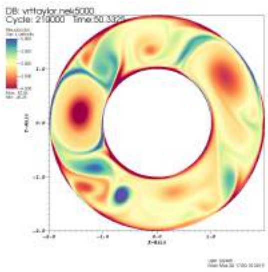

(F) $t = 50.33$ s

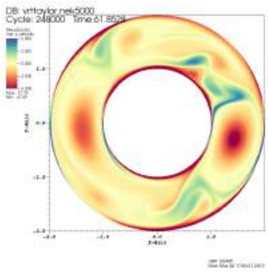

(G) $t = 61.85$ s

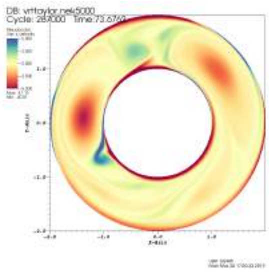

(H) $t = 73.67$ s

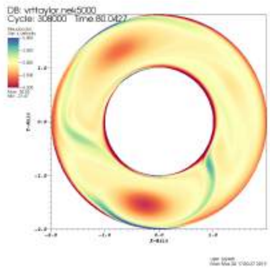

(I) $t = 80.04$ s

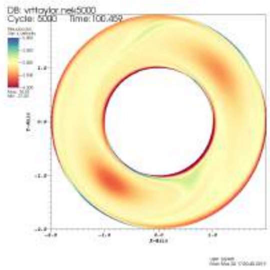

(J) $t = 100.459$ s

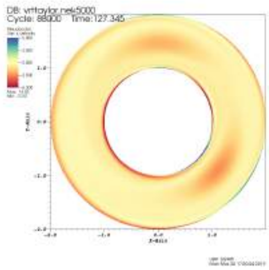

(K) $t = 127.345$ s

FIGURE 5.9: Vorticity profile at subsequent times at $Re = 3000$, $k = 5$

The energy plot in this case, as shown in figure 5.10 clearly shows the lowest energy is way below the laminar energy, and stands at 0.8611 non-dimensionalised to the laminar energy. this is 14% lower than the energy of laminar flow, which is significant enough to study further. This energy is reached at 97.33s, or 15.49 revolutions of the inner ring. After this, the energy begins to increase further and reaches 88% of laminar energy at 139s, or 22.12 revolutions of the inner ring, where the case was stopped. The increase to the laminar solution is slow and therefore the case is stopped. The dependence of energy on initial state and Reynolds Number seems to be evident, although the relationship between the two is not clear to us at this point. Further analysis is needed to reach a conclusion for the same.

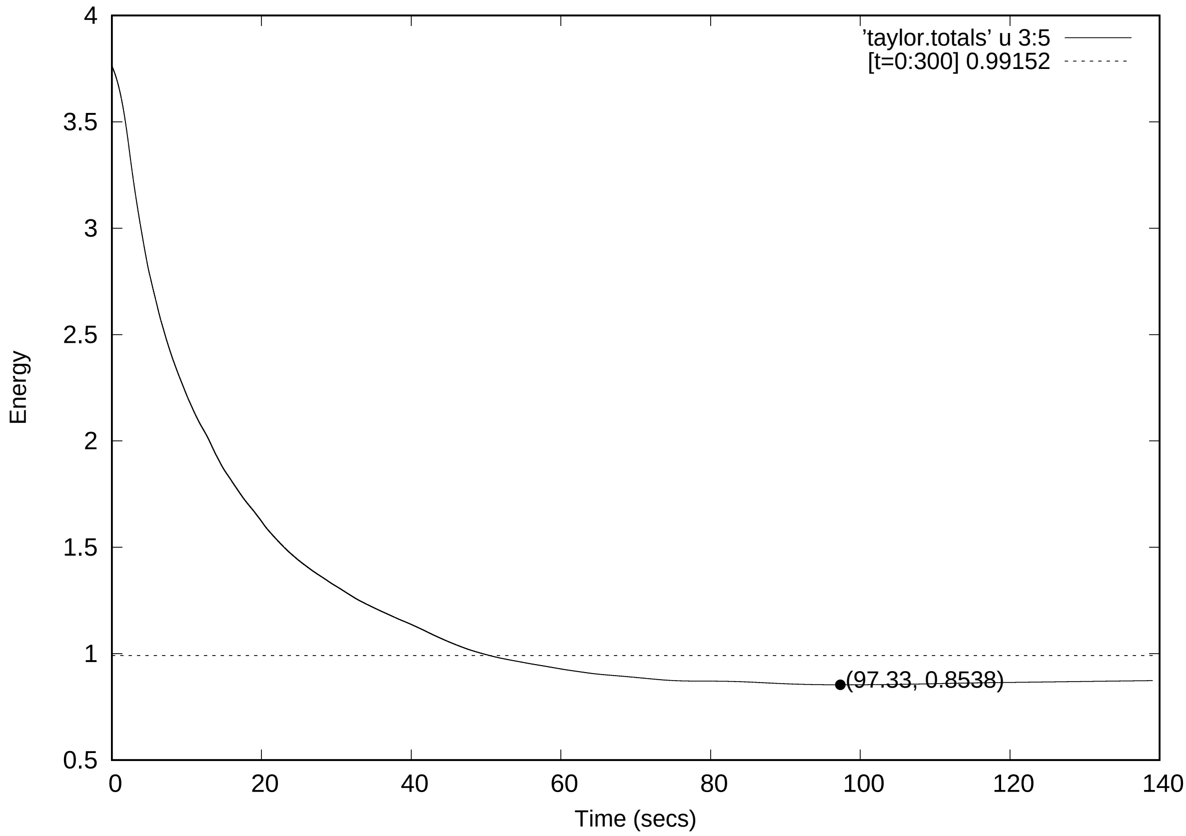

FIGURE 5.10: Energy inside the domain, $Re = 3000$ $k = 5$

5.3.2 Initial Energy 12.158

When looking at results for Re 3000, at the higher initial energy, a clear similarity can be seen in the macroscopic properties to Re 1000 at the higher IE, but it is hard to establish clearly how this is related to the case at Re 3000 at the lower IE. This implies that ICs change the case a lot more than just Reynolds' number can. The evolution of vorticity over time is very similar, although the vortices last longer in this case, and that can be explained by the fact that a vortex loses its energy to viscosity, and increasing Reynolds' number decreases the viscosity, so it takes longer to see the vortices disappear. This statement would become clearer in the results of the next run, as it would show the dependence of time to reach minimum energy on the Reynolds' number.

The vorticity evolution is shown in figure 5.11, and is explained here. Initially, the higher energy IC helps generate vortices through the inner and outer rings, the most prominent of which is the one formed at the inner ring in the lower half of the ring. These strong vortices in 5.11a can be seen at the bottom of the ring. As they continue to rotate, two sets of vortices on the opposite side of the ring can be seen in figure 5.11b. By 28 seconds, most of the secondary and weaker vortices get skewed and then disappear, and only four negative and one positive vorticity spots can be seen, in 5.11d, where one cyclone and one anticyclone are very close to each other. When vortices are close to each other, they skew the edges of each other, and when a vortex

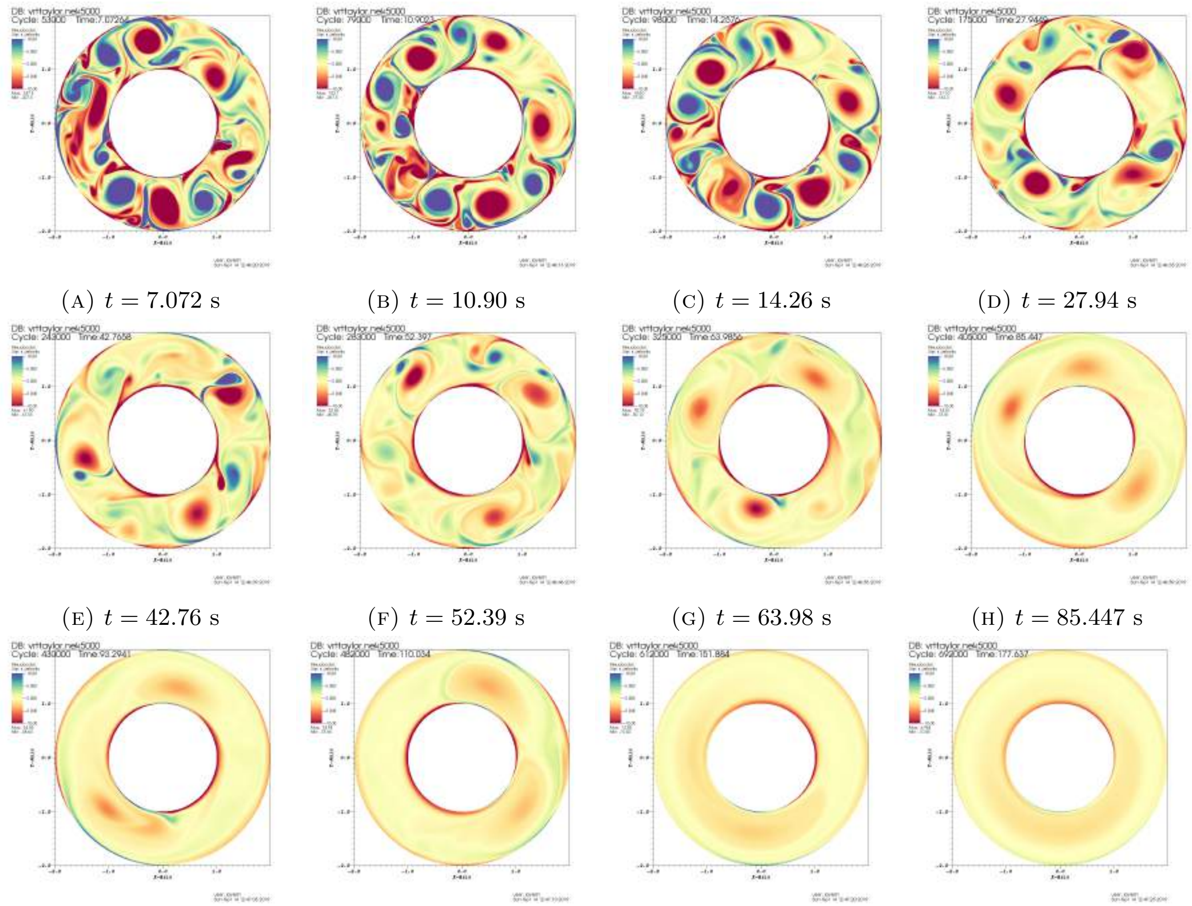

(A) $t = 7.072$ s (B) $t = 10.90$ s (C) $t = 14.26$ s (D) $t = 27.94$ s

(E) $t = 42.76$ s (F) $t = 52.39$ s (G) $t = 63.98$ s (H) $t = 85.447$ s

(I) $t = 93.29$ s (J) $t = 110.034$ s (K) $t = 151.884$ s (L) $t = 177.64$ s

FIGURE 5.11: Vorticity profile at subsequent times at $Re = 3000$, $k = 10$

gets skewed or stretched, it loses its energy to vorticity much faster, and therefore that vortex can be seen to not be present in figure 5.11e. As time progresses, the strength of vortices keeps getting reduced, and at this time two interesting phenomena can be oberved with respect to the reinforcement and destruction of vortices. The vortex streaks in the flow produce several weak vortices of both, cyclone and anticyclone nature, but when the anticyclone comes in contact with the bigger anticyclone, or a cyclone comes in contact with a bigger cyclone, they reinforce each other to form a larger vortex. However, when opposite signs of vorticity interact, the opposite happens and the vortex decomposes slowly. As time passes, the vorticity decreases constantly, and the strength of vortices goes down.

Something interesting happens in figure 5.11h, where two vortices can be seen, and one of them is faster than the other, almost approaching it to mix and reinforce each other. A short while later, in figure 5.11i, it can be seen that the two vortices merge to for a larger vortex, which in the subsequent time merges with the other anticyclone, as these vortices continue to die. minimum energy is reached between 5.11j and 5.11k at 124.24 seconds. After this, the vortex streaks also slowly disappear and the return to laminar flow takes place.

When looking at the energy of this case, we can see that the energy in this case, as in all the others, decays and then after reaching a minimum begins to increase. At Re 3000 with the

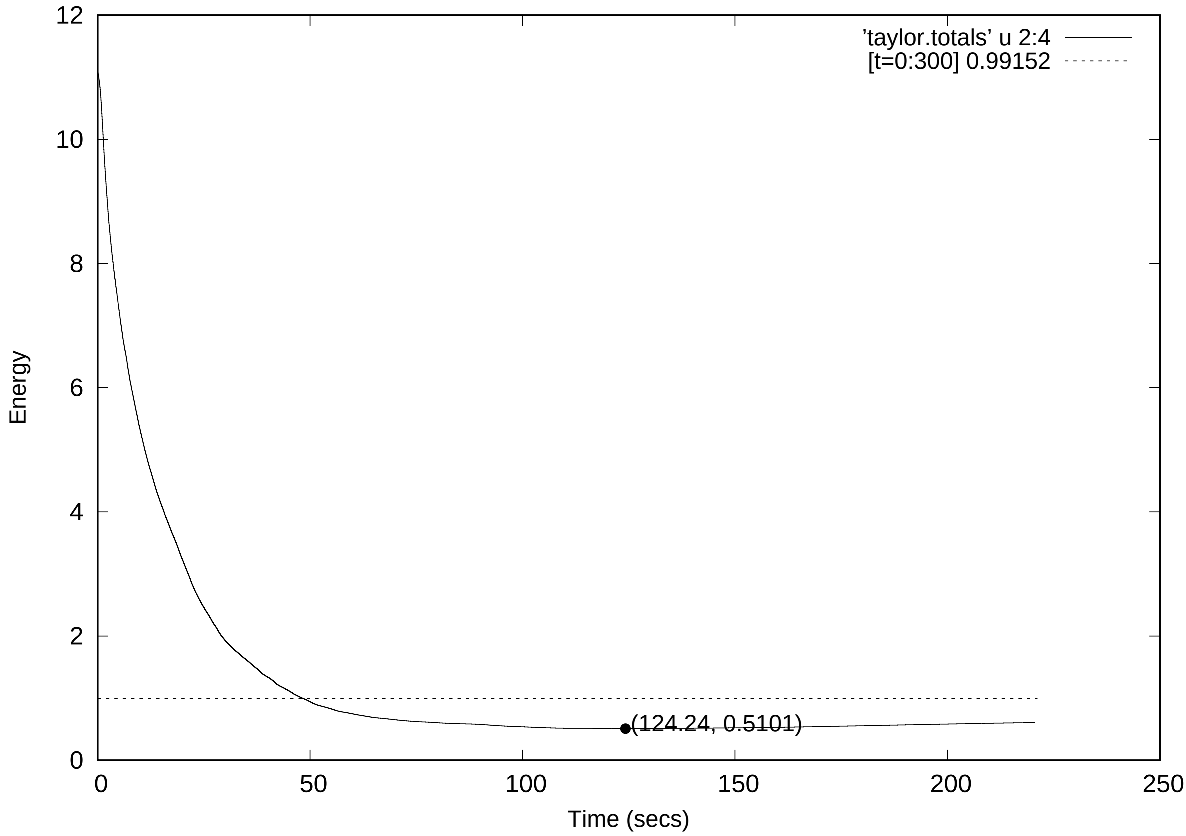

FIGURE 5.12: Energy inside the domain, $Re = 3000$ $k = 10$

higher IE, the minimum energy reached is 0.5101 normalised to the energy of laminar flow, ie 51% of laminar energy. This is significantly less than that in case of the lower IE, but in line with the energy observation in case of Re 1000 with the higher IE. Also, this energy is reached at 124.24 seconds, or 19.77 rotations of the inner ring (non-dimensional time). This is more than that in any cases observed before, but in stark opposition to the case of Re 1000, where the higher IE reached the minimum energy level in a shorter time. This implies that in case of Re 1000 the rate of energy decay is higher than that in case of Re 3000, but why the time for the lower IE to reach the minimum energy is lesser is still not known. At this point we hope to see a clearer pattern when higher Re results are seen, so that discussion has been left for later.

5.4 At Reynolds' Number 5,000

5.4.1 Initial Energy 3.862

As in case of Reynolds' number 5000, and the initial energy of 3.86 normalised units, which is given by $K = 5$, the results for vorticity can be seen in the figures 5.13a to 5.13j. What happens in this case is again surprising, when seen against the results from $Re = 1000$, as the same anticylone vortex which is seen there is also seen here, but is one of the first vortices to die. As the solution progresses through time, the results can be seen even more clearly. In

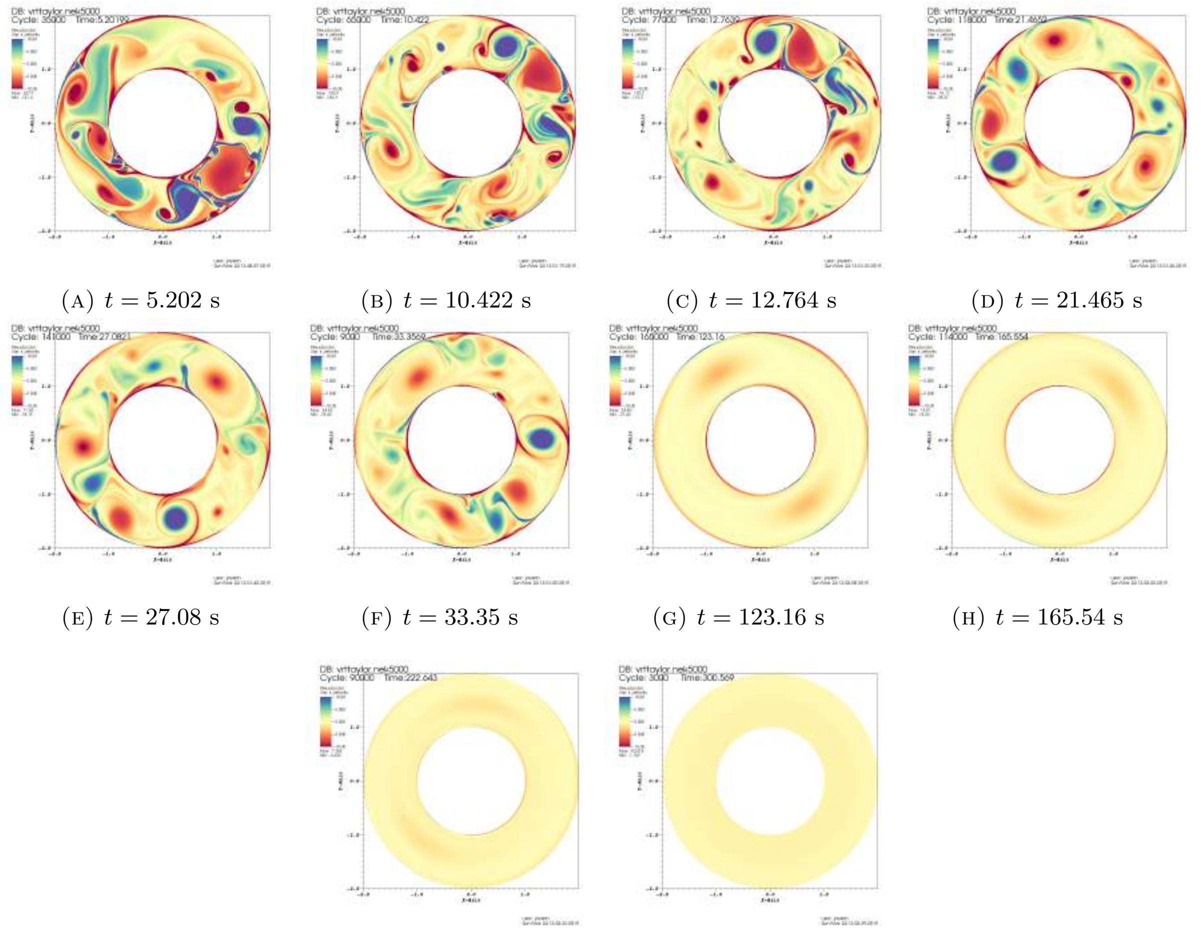

(A) $t = 5.202$ s (B) $t = 10.422$ s (C) $t = 12.764$ s (D) $t = 21.465$ s

(E) $t = 27.08$ s (F) $t = 33.35$ s (G) $t = 123.16$ s (H) $t = 165.54$ s

(I) $t = 222.643$ s (J) $t = 300.57$ s

FIGURE 5.13: Vorticity profile at subsequent times at $Re = 5000$, $k = 5$

figure 5.13a, the first large vortex can be seen, which is the same as in $Re = 1000$, but the magnitude of vorticity of this vortex is less than the maximum vorticity in the domain, unlike the previous case. The same prominent anticyclone continues to rotate, but can clearly be seen losing energy in figures 5.13b and 5.13c. In 5.13d, it becomes extremely less prominent, and cyclones in the domain gain prominence. As time passes, the earlier not so significant vortex streaks become important, as they have in 5.13d. As time goes on, the vortices lose energy to the point where they have either disappeared or are about to disappeared, and have skewed in shape to an extreme degree. Even in this stage, the vortex streaks are still very prominent, and can be seen in figure 5.13g. With the progress of time, even these vortex streaks disappear and the vorticity reaches its laminar value, which happens after $t = 300$ s, which is the last timestep considered for the run. At $Re = 5000$, the time for relaxation to 95% laminar energy is much more, although the run was stopped at 325s of physical time, at which the case was at 89.5% towards the laminar solution.

The most interesting observation in this case is that even at $Re = 5000$ at $k = 5$, the anticyclone survives till the end, which is the same as in case of $Re = 1000$. Another very interesting observation is in case of the variation of Energy with time, which is given as shown in the figure 5.14.

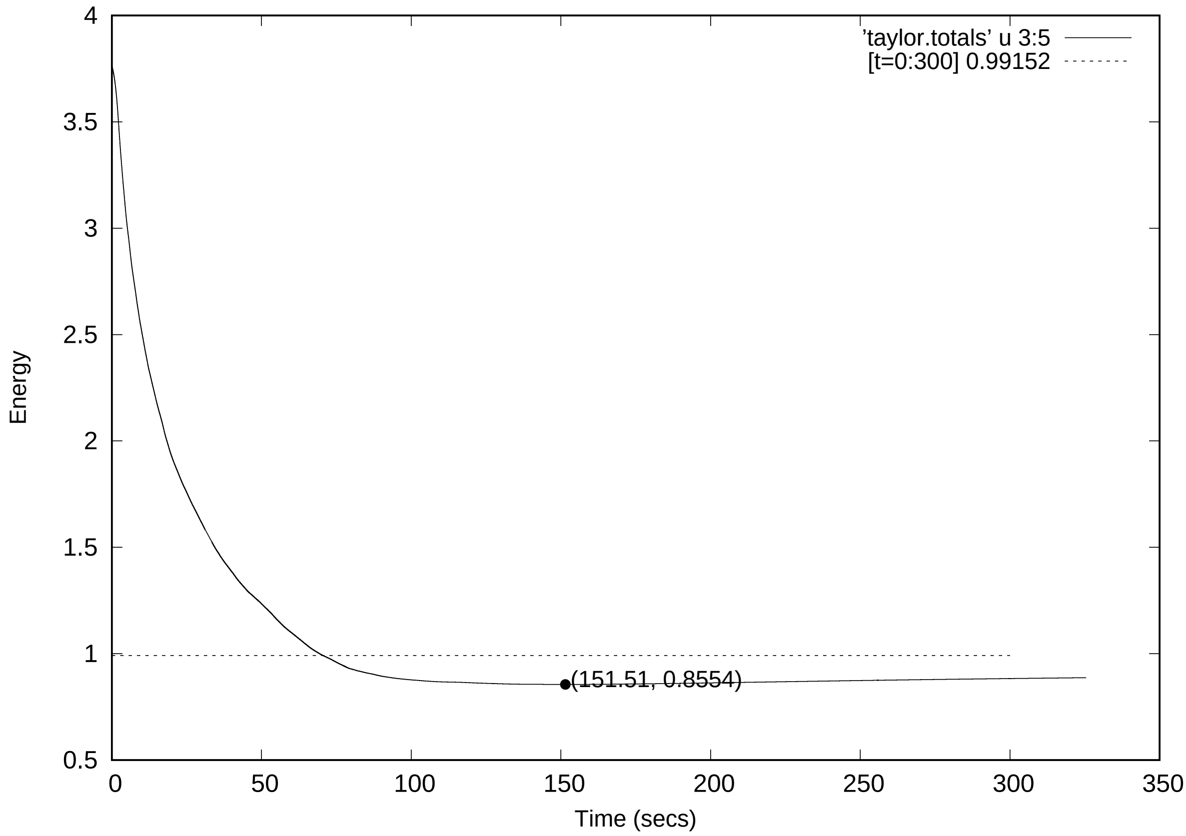

FIGURE 5.14: Energy inside the domain, $Re = 5000$ $k = 5$

As the variation makes amply clear, the minimum energy goes down to 0.8617 normalised units, which occurs at $t = 151.51$ s, which is at 24.11 revolutions of the inner ring in non-dimensional time units. The time to recover from this minimum state is also huge, as the case reaches only 89.5% laminar energy at 325.44 s (51.79 revolutions).

5.4.2 Initial Energy 12.158

In this evolution as well, the inner ring produces multiple vortices, and as can be seen in figure 5.15c, the vortices interact with each other, and get skewed and destroyed very quickly. This can be seen in the figure at around 270°, and as the ring continues to rotate, the figure 5.15e shows how the vortices get stretched while getting destroyed. The cyclone and anticyclone vortices interact with each other to very quickly reduce the vorticity across the domain, and at around 48 seconds, it can be seen that only three anticyclones can be seen, one of which is also evidently interacting with a cyclone and stretching even further. These interactions can also be seen in the further timesteps. However, in this case, contrary to the previous ones, a clear last surviving vortex cannot be observed. The prominent vortices are both, cyclone and anticylcone, upto a very late point in time. In this case, the streaks also play a much greater role, as they generate more and more vortices which interact with each other and either reinforce or destroy the vortices, as explained earlier. as can be seen in figure 5.15i, there is no prominent vortex as clearly visible as in the previous cases, however, it can be seen that the cyclone is prominently

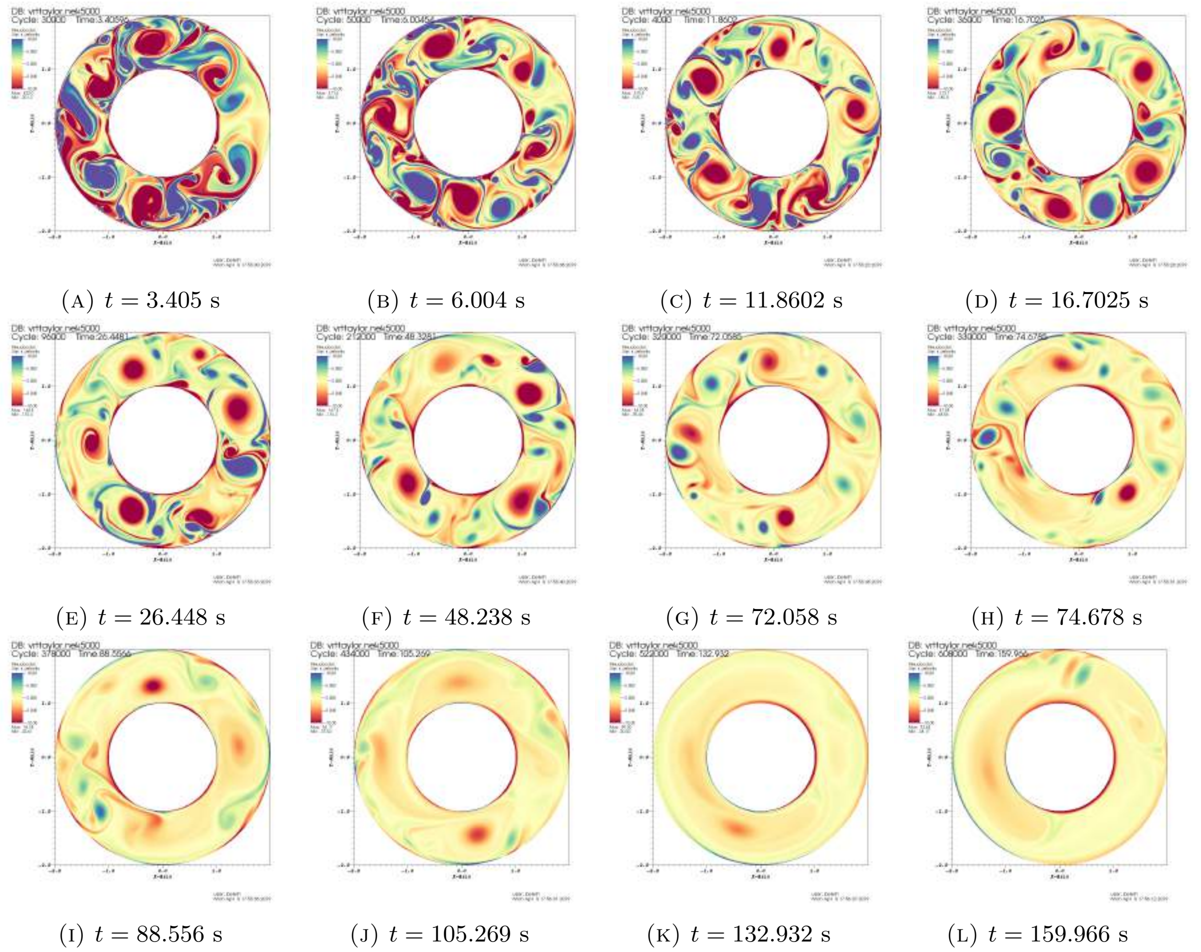

(A) $t = 3.405$ s (B) $t = 6.004$ s (C) $t = 11.8602$ s (D) $t = 16.7025$ s

(E) $t = 26.448$ s (F) $t = 48.238$ s (G) $t = 72.058$ s (H) $t = 74.678$ s

(I) $t = 88.556$ s (J) $t = 105.269$ s (K) $t = 132.932$ s (L) $t = 159.966$ s

FIGURE 5.15: Vorticity profile at subsequent times at $Re = 5000$, $k = 10$

surrounded by skewed anticyclones, and anticyclones are surrounded by skewed cyclones. This helps in generating even more vortices from the streaks, and in figure 5.15j, one clear anticyclone seems to survive, along with another faint anticyclone surrounded by vorticity of the opposite sign. As time progresses, as seen in figure 5.15l, the new vortices interact and die one after the other, and a very faint anticyclone, extremely stretched by this point, is the last one surviving. What is interesting to note here is that there is no prominent vortex that dominates the domain, unlike what had been seen in the previous cases.

In case of the energy evolution, the minimum energy is 0.4960 nondimensional units, which is also the first time that that the minimum energy falls below half the laminar value. This energy is reached at 190.04 seconds, or 30.24 rotations of the inner ring. Another trend that can be observed in the Re 5000 case is that the time to reach minimum energy for the lower IE is still less than that for the higher IE, which is intuitive and also the same as in the case of Re 3000.

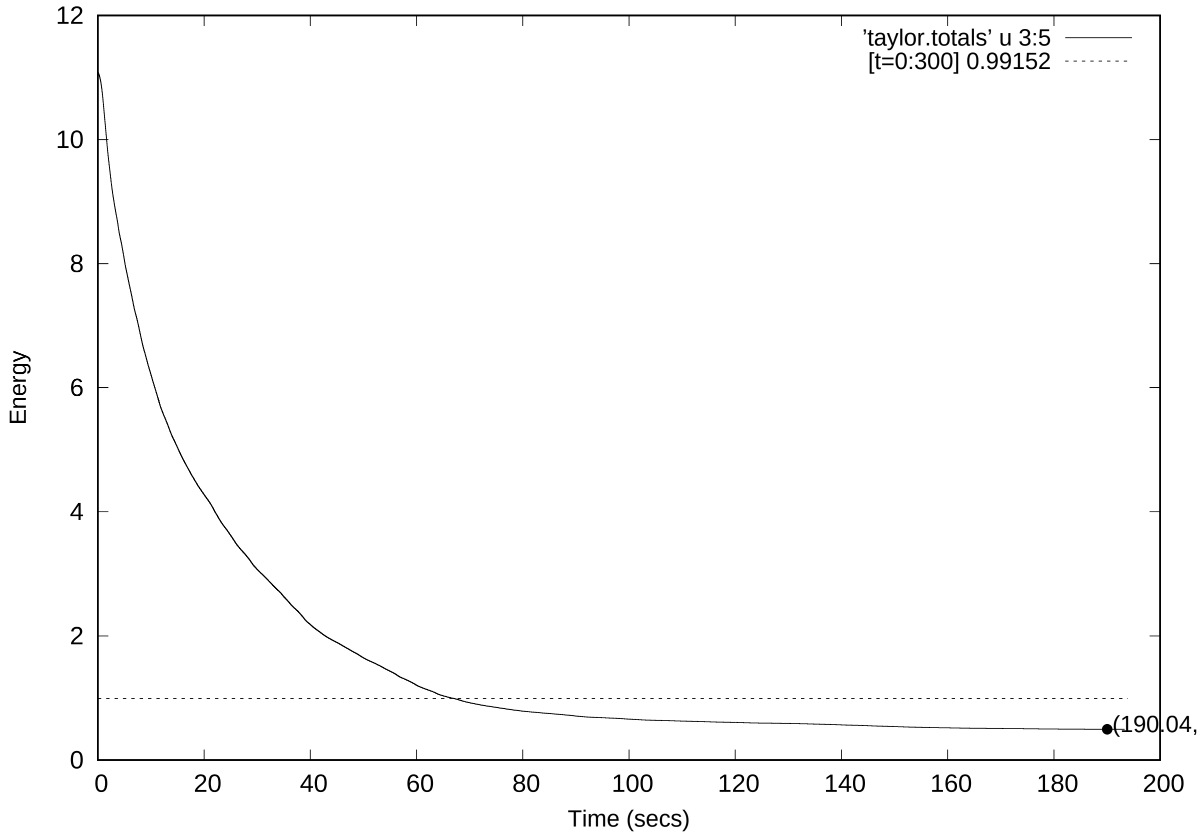

FIGURE 5.16: Energy inside the domain, $Re = 5000$ $k = 10$

5.5 At Reynolds' Number 10,000

5.5.1 Initial Energy 3.862

In case of Reynolds' Number 10,000, we can initially see how the vortices are generated, and a key feature to be observed is how the size of the smaller vortices further decreases, and their number increases as viscosity decreases. Moreover, in 5.17b, it can also be seen how a large cyclone destroys an anticyclone, somewhat like devouring it, and in the process losing some energy of its own. The anticyclone is the bigger red vortex as can also be seen in 5.17a. As time progresses, we can see similar trends to the previous cases, with vorticity decreasing and the number of vortices decreases with time. However, even more vortices are generated through the streaks in this case, and the interaction of the vortices is even more prominent. As can be seen in 5.17f, the vortex interactions through which cyclones are strengthened can be seen. The distorted blue vortex reinforces the larger blue next to it, and that makes the cyclone even stronger. Another qualitative parallel can be drawn to the case at Re = 5000, k = 10, that the structure eventually is dominated by cylcones, which is in stark contrast to the one seen in lower Reynolds' numbers. As time progresses, the effect of streaks generating vortices which reinforce the dominant cyclones plays a vital role in helping the vortices survive for much longer, but as they lose energy while rotating, they eventually die down. What is more interesting though, is that despite the vortices being really close to each other from around 5.17h, and being in the

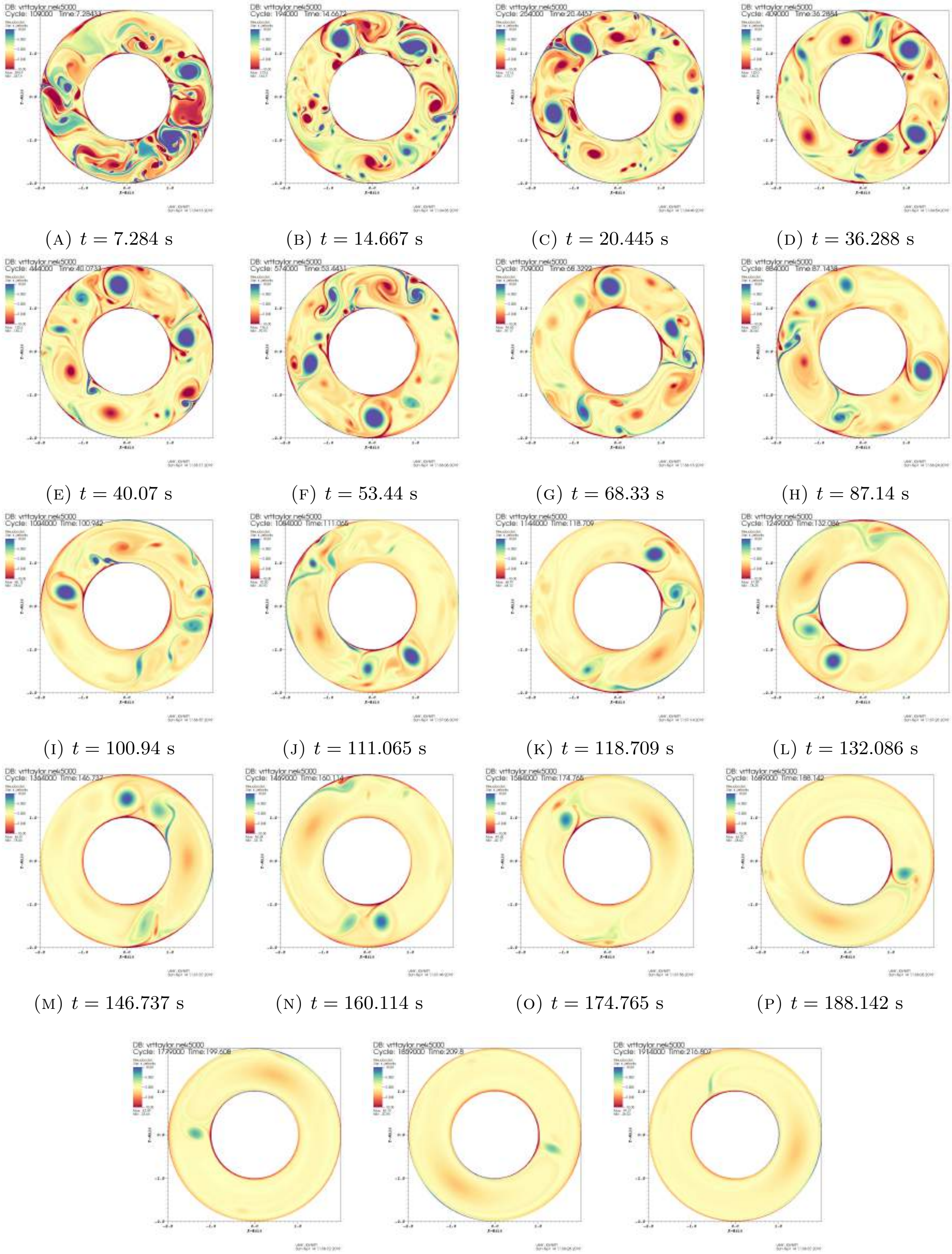

(A) $t = 7.284$ s (B) $t = 14.667$ s (C) $t = 20.445$ s (D) $t = 36.288$ s

(E) $t = 40.07$ s (F) $t = 53.44$ s (G) $t = 68.33$ s (H) $t = 87.14$ s

(I) $t = 100.94$ s (J) $t = 111.065$ s (K) $t = 118.709$ s (L) $t = 132.086$ s

(M) $t = 146.737$ s (N) $t = 160.114$ s (O) $t = 174.765$ s (P) $t = 188.142$ s

(Q) $t = 199.608$ s (R) $t = 209.8$ s (S) $t = 216.80$ s

FIGURE 5.17: Vorticity profile at subsequent times at $Re = 10000$, $k = 5$

same direction, they do not merge until a much later stage to for one strong vortex, and in the meanwhile, the leading vortex has lost much of its energy. This merging, however, takes place at around $t = 168s$, and can be seen as the difference between figures 5.17m and 5.17n.

The minimum energy in this case is reached in between states 5.17l and 5.17m, at 151.51s (24.11 non-dimensional units). This is between the vortices merging and the disappearance of smaller vortices. What is also to be noted is that the overall vorticity of laminar flow is reached much later, but the case is stopped at 220s in the interest of compuational time. Even in this case, the time to minimum energy is surprisingly larger than that for Re = 5000 for the similar initial energy.

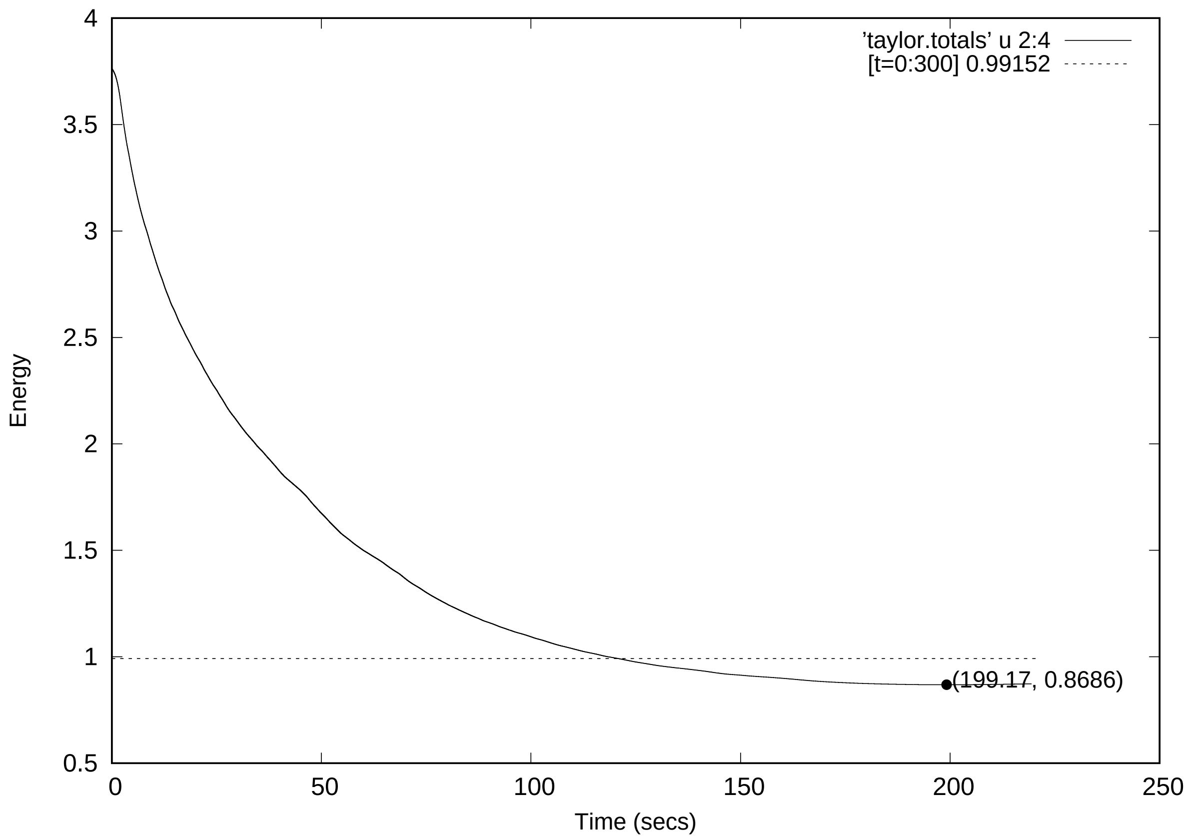

FIGURE 5.18: Energy inside the domain, $Re = 10000$ $k = 5$

5.5.2 Initial Energy 12.158

When looking at the profiles for Re = 10,000 with the higher energy, it is important to keep in mind the profiles for the previous case, with the lower IE. The reason for this is to see the similarities and differences in these plots, which would soon become obvious. At first glance, it can be seen from figures 5.19a to 5.19d that a large number of initial vortices are formed, which them give way to three large cyclones and one anticylcone, along with several other less prominent vortices. as time progresses, at 53.51s, as seen in figure 5.19f, the number of promienent cyclones has increased to five, while two anticyclones prevail next to each other. As

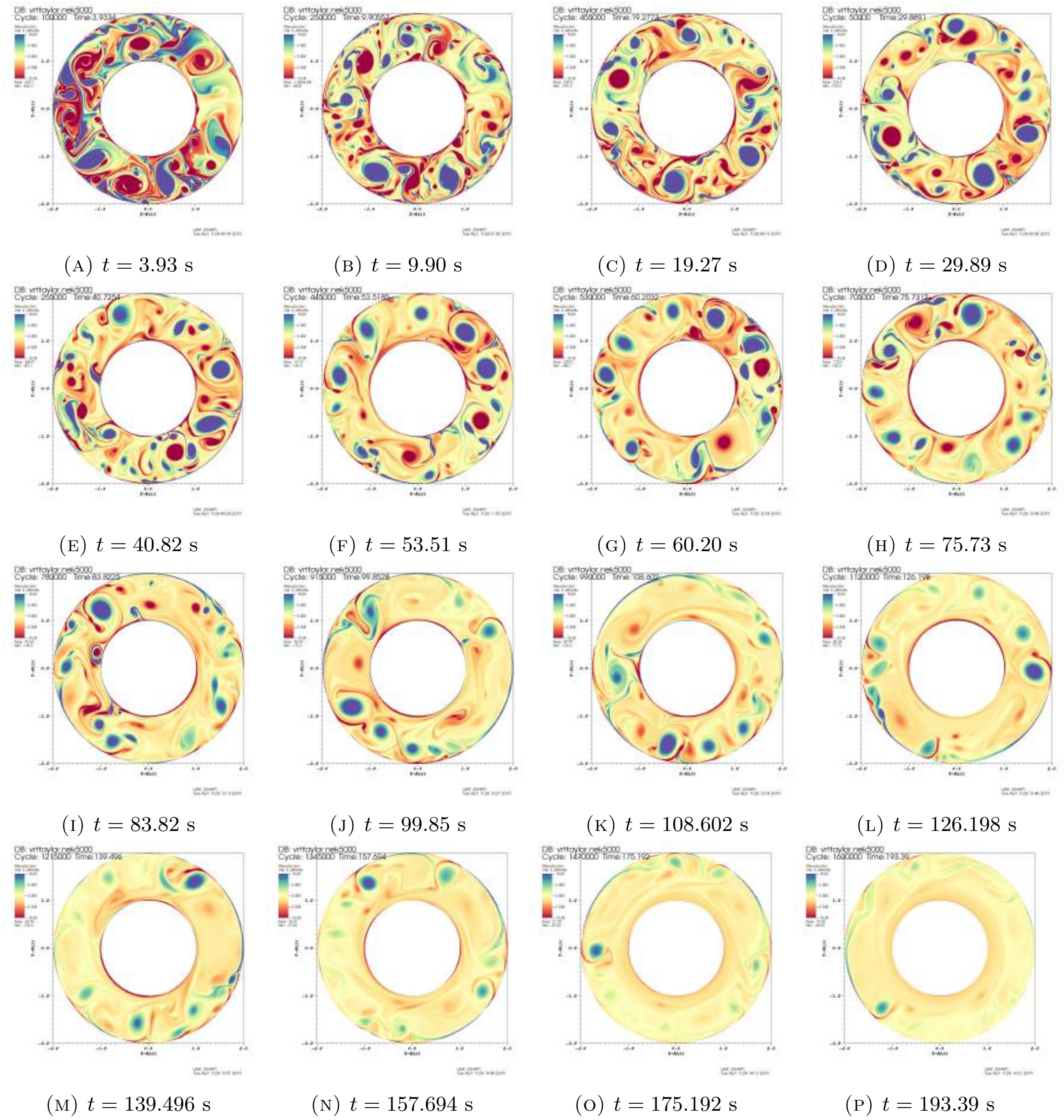

(A) $t = 3.93$ s (B) $t = 9.90$ s (C) $t = 19.27$ s (D) $t = 29.89$ s

(E) $t = 40.82$ s (F) $t = 53.51$ s (G) $t = 60.20$ s (H) $t = 75.73$ s

(I) $t = 83.82$ s (J) $t = 99.85$ s (K) $t = 108.602$ s (L) $t = 126.198$ s

(M) $t = 139.496$ s (N) $t = 157.694$ s (O) $t = 175.192$ s (P) $t = 193.39$ s

FIGURE 5.19: Vorticity profile at subsequent times at $Re = 10000$, $k = 10$

time progresses, these vortices continue to interact with each other, and the vortices rotating in the same direction reinforce each other, while those in the opposite direction destroy each other, until in figure 5.19j, onnly a few prominent cyclones remain, while most anticyclones die down. As time progresses, even these vortices lose energy to viscosity, as had been described previously. This gives rise to the final state as seen in figure 5.19p, where there are very small vortices, and most have died down. The state of least energy, however, has not been reached, which it does at around 202.19s, when a very small cyclone vortex is left, and the laminar velocity begins to emerge.

The minimum energy in this case is at 0.4886 (normalised to laminar energy), and is the least seen so far in any case, therefore we can conclude safely that the trend of minimum energy

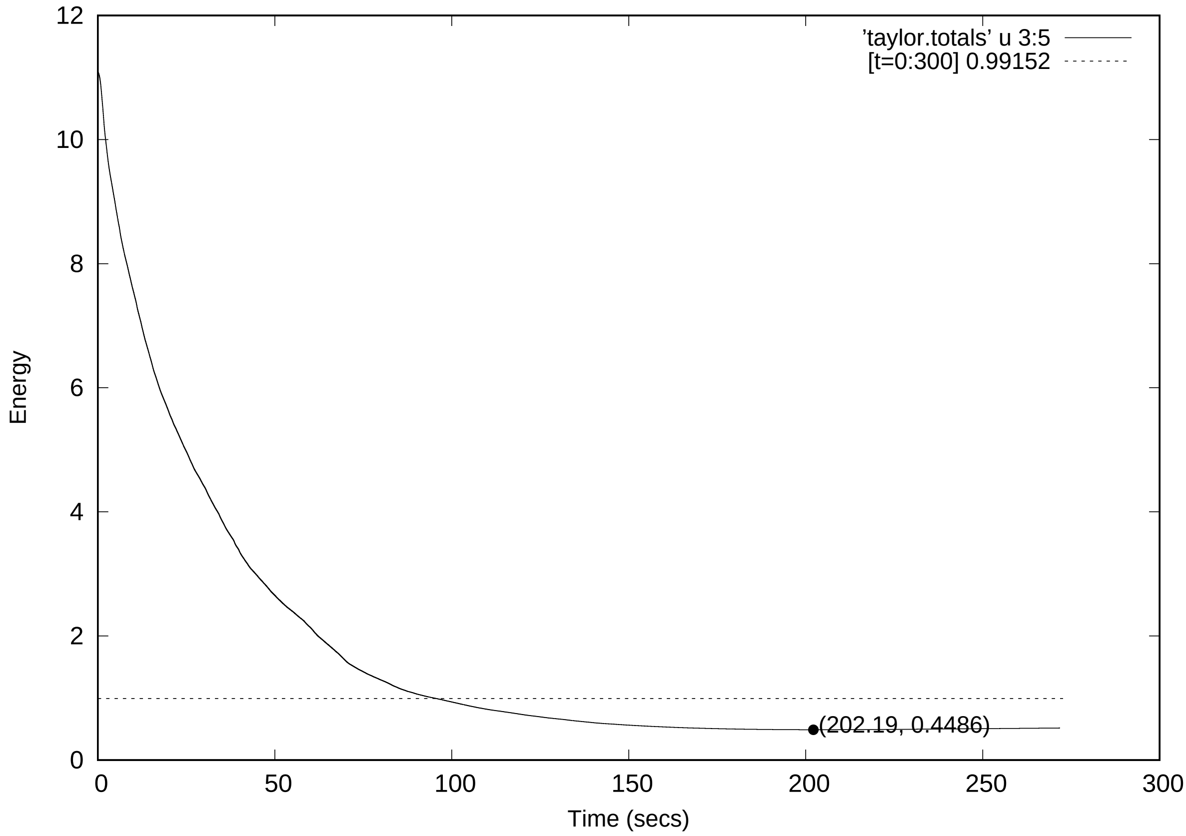

FIGURE 5.20: Energy inside the domain, $Re = 10000$ $k = 10$

decreasing with increase in Reynolds' number is clear. This energy occurs at 202.19s, or 32.18 revolutions. Although this is very close to the value established at Re = 5000, it is still greater than that, so time to laminar flow also increases with increase in Re.

Chapter 6

Conclusions

6.1 Summary of Minimum Energy

As it can clearly be seen from these results, the minimum energy is always lower than the analytical energy of laminar flow. The entire data has been normalised to the laminar energy, and therefore the energy of laminar flow is 1. As it can also be seen, there is not much variation from Re = 3000 to 10000, for the lower initial energy (3.86× laminar energy). This trend is also followed in the higher initial energy, although what can be qualitatively said is that the time to reach minimum energy increases with Reynolds number, and with initial energy.

We also postulate that the minimum energy being less than the laminar energy can be attributed to a slow down in the overall velocity of the flow, which is caused due to the action of the vortices. In order to confirm this idea, we plotted the azimuthal velocity averaged iver all angles, for all values of R in the grid. Since the analytical plots themselves do not have a radial velocity, the plots for the radial velocity just show the locations of the surviving (very faint) vortices. The plots obtained by this process are shown in figure 6.2.

Based on this information, we arrive at a hypothesis, enumerated in the next section.

Reynolds Number	$E_{in} = 3.86$		$E_{in} = 12.16$	
	E_{min}	t_{min}	E_{min}	t_{min}
1k	0.973	12.09	0.587	8.85
3k	0.861	15.49	0.5101	22.12
5k	0.862	24.11	0.496	30.24
10k	0.868	31.69	0.4886	32.18

Table 6.1: Summary of Minimum Energy and Time for different ICs

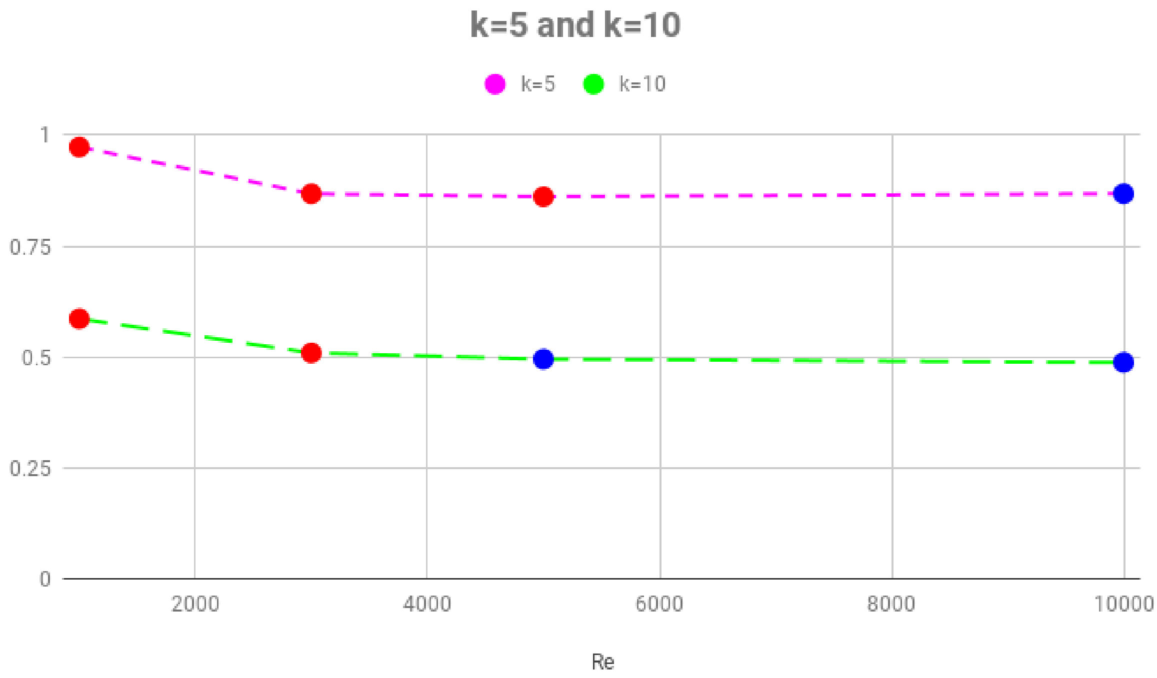

FIGURE 6.1: Results for E_min vs Re and Initial Energy

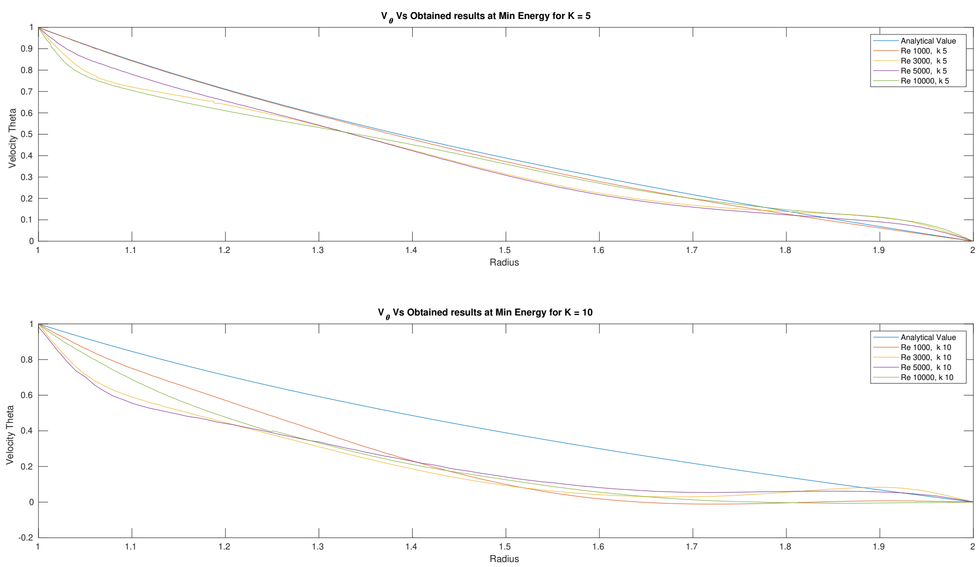

FIGURE 6.2: V_θ vs R for both Initial Energies and all Re

k \ Reynolds Number	1000	3000	5000	10,000
5	15.79	9.835	9.63	6.925
10	18.22	12.63	9.44	7.86

Table 6.2: Average width of sepratices at different Re

k \ Reynolds Number	1000	3000	5000	10,000
5	4.85E-05	5.34E-05	5.20E-05	6.61E-05
10	2.67E-05	4.13E-05	6.79E-05	5.21E-05

Table 6.3: timescales at different Re

6.2 Timescales

We can see that time increases with Re, and say that time is dependent on a variation of a typical length scale and viscosity. For vortices, we know this scale to be:

$$t \propto \frac{l^2}{\nu} \implies t \propto l^2 \times Re \implies \frac{t}{l^2 Re} = K \tag{6.1}$$

Where K is any constant. So when we try this at with the case files available at hand, we see that the vortices of all sizes produce sepratices of different length scales, which are averaged for 5-6 sampling points per case file. The width of sepratices (in pixels), observed and measured from the vorticity plots is given in table 6.2.

When this is used to calculate the parameter $\frac{t}{l^2 Re}$, the results are as given in table 6.3. The same data is also plotted in figure 6.3.

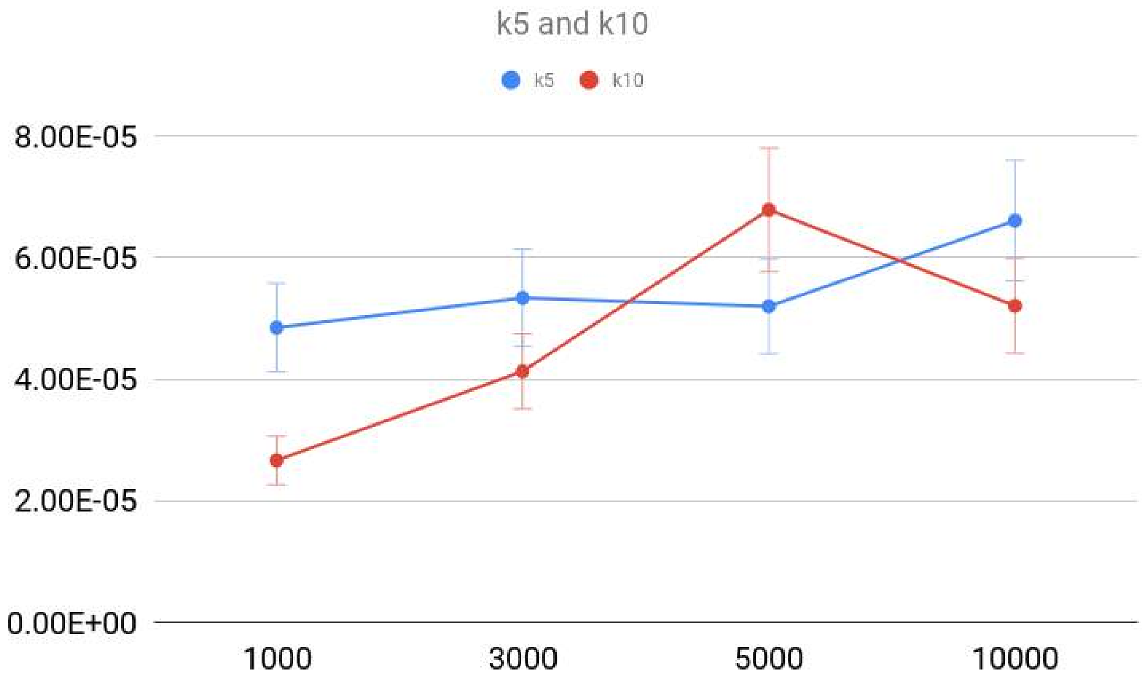

FIGURE 6.3: Timescales for all Re and IEs

6.3 Summary of Significant Conclusions

- All flows observed, at all Reynolds' numbers, relax to laminar flow.
- In the process to reach laminar flow, flows reach a minimum energy state, less than the laminar energy.
- The minimum energy initially decreases with increase in Re, and then becomes steady.
- Minimum energy state is not of zero vorticity, but no prominent vortices exist.
- Minimum energy is lower for higher initial energy, which is likely related to the fact that higher energy produces more turbulence which provides more drag that slows down the flow. This is also supported by the plot obtained in figure 6.2.
- Time to laminar flow increases with Re, but slower than linear, which would be expected in case of linear relaxation.
- Within the assumed margin of error, the time to minimum scales to square of length scale and Re.
- The dependence on initial energy was not deemed feasible due to insufficient data points.
- Last surviving vortices are anticyclone for Re 1000 (both IEs), 3000 (both IEs) and 5000 (lower IE), neither clear cyclone nor anticylcone for Re 5000 (higher IE), and cyclone for Re 10,000 and 20,000 (both IEs). The cause of this is yet not known.

Appendix A

Movies of Evolution

A.1 Movie Links

The Videos of evolution are given in the following links:

- Reynolds' Number = 1000
  - k = 5
  - k = 10
- Reynolds' Number = 3000
  - k = 5
  - k = 10
- Reynolds' Number = 5000
  - k = 5
  - k = 10
- Reynolds' Number = 10000
  - k = 5
  - k = 10

Bibliography

[1] Illinois Argonne National Lab. *Nek5000 version 17.0.* Available: https://nek5000.mcs.anl.gov., 2018.

[2] M.O. Deville, P.F. Fischer, and E.H. Mund. *A spectral element method for fluid dynamics : laminar flow in a channel expansion.* Cambridge University Press, 1984.

[3] G. Falkovich. *Fluid Mechanics.* Cambridge University Press, 2018.

[4] G. Falkovich and N. Valdimirova. “Inertial Ranges in Two-Dimensional Turbulence”. In: *Physical Review Letters* 121 (Oct. 2018), pp. 164501–1–164501–5. URL: `10.1103/PhysRevLett.121.164501`.

[5] Robert H. Kraichnan. “Inertial Ranges in Two-Dimensional Turbulence”. In: *The Physics of Fluids* 10 (July 1967), pp. 1417–1423. URL: `https://doi.org/10.1063/1.1762301`.

[6] A.T. Patera. “A spectral element method for fluid dynamics : laminar flow in a channel expansion”. In: *Journal of Computational Physics* (July 1984), pp. 468–488.

[7] Stephen B. Pope. *Turbulent Flows.* Cambridge University Press, 2000.